Phase behavior of colloidal dispersions in shear flow

M. Paul Lettinga
(Dated: October 6, 2014)

I. INTRODUCTION

One of the key tasks in physical chemistry is to predict whether dispersions are stable, meta-stable or unstable so, in other words, to predict the phase diagram. The factors that determine the stability are the interaction between the particles that constitute the dispersion and their shape. The beauty of colloid science is that colloidal chemistry can be used to exactly program the interaction between particles and their shape: particles with all kind of shapes can be made attractive, repulsive or hard core-like. In addition, colloids are experimentally easily accessible since their size is typical of the order of visible light, so that the light scattering and microscopic techniques can be used to probe the systems. Thus thermodynamic theories based on particle-particle interactions can be used to calculate phase diagrams, which can be readily tested experimentally. While this explains why colloidal dispersions are popular in fundamental research, they are also of huge practical interest, since many examples can be found in daily life. Standard examples are blood, paints, and dairy products, but the list is inexhaustible. Colloidal dispersion thus are a core class of Soft Matter materials.

The main characteristic of soft matter systems is the ease with which they can be perturbed, since the interactions are of the order of 1 kT. As a consequence, when studying phase behavior extreme care needs to be taken that the systems are not perturbed by for example tumbling, vibrations, temperature gradients, EM fields, gravity etc. In the real world of industrial processing, cosmetic and food industry, biology, etc. soft matter systems will often be exposed to external fields. The question is whether the stability and structure of the colloidal dispersions change, and therefore phase diagrams, when systems are subjected to an external field. The most prominent external field is shear flow, because any motion of the sample will most likely induce shear flow. Flow can be desirable when material is transported from A to B. A good example here is blood circulation, where highly concentrated dispersions of more or less deformable cells are pushed through narrow channels [1]. Flow can be partly wanted and partly unwanted as is the case for paints for which the flow behavior sets the final product as well as the pathway to get there [2]. Sometimes there is no control as can be the case when putting tomato ketchup on a hamburger. Sheared colloidal dispersion are also of fundamental interest. First, the interplay between thermodynamic instabilities and hydrodynamic instabilities guaranties a plethora of novel effects, see Ref. [3] for an extensive introduction. Second, shear flow perturbs the interaction between the particles and with that also the phase behavior. Understanding both aspects on a fundamental level will in return give insights in practical questions regarding the force that is needed to shear a sample and the stability of the resulting flow.

The goal of this chapter is to give the reader a flavor of the complexity of sheared colloidal dispersions. We will do this on the hand of a few examples for which it is at least to some extend possible to do theory so that theory and experiments can be compared. For each example we will first describe the equilibrium phase behavior, and then show how this phase behavior is affected by shear flow. Thus, non-equilibrium phase diagrams will be constructed indicating where the different phases are located as a function of the relevant parameter like the colloid concentration or interaction and the shear rate. We will also discuss how this non-equilibrium phase behavior perturbs the flow behavior of the system including flow instabilities.

We will discuss systems with increasing degree of complexity. We will start with dispersions of colloidal hard spheres, which form the benchmark of colloidal science. This system undergoes a phase transition from the liquid phase, where the Brownian particles are disordered, to a crystalline state, which takes place at a volume fraction of 49 %. At even higher concentrations, for volume fractions larger than 0.58, the system will be structuraly arrested and form a glass, which will be discussed in Chapters 12 and 13. When the liquid phase is subjected to shear flow already many interesting features are observed such as the divergent viscosity with increasing concentration [4], which is relevant for blood rheology[5], and extreme shear thickening [6], as used for body armor [7]. We will focus however on the *effect of shear flow on the crystallization of colloidal spheres*, that will be discussed in III. We will exploit here the fact that colloidal spheres can be charged and therefore repulsive, so that the crystallization takes place at lower concentrations.

Colloidal spheres can also be made attractive, either by grafting them with a small polymer layer for which the solvent conditions can be tuned by temperature or pressure, or by adding small polymers in the solution which push the colloids together due to an osmotic pressure imbalance, the depletion force, **see Chapter ???**. Attractive colloids can undergo a gas-liquid phase separation, just as a van der Waals gas, resulting in a top phase with a colloid poor top phase and a colloid rich bottom phase. The critical fluctuations just before phase separation sets in are slow and

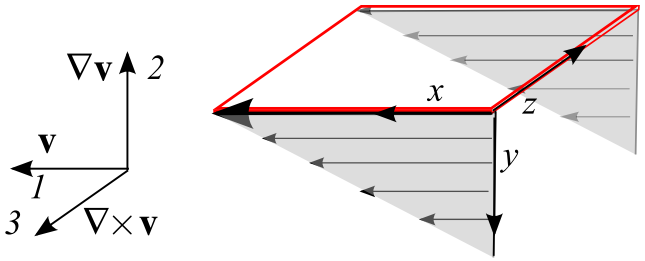

Figure 1: Definition of the shear directions: 1, flow direction; 2, gradient direction; 3, vorticity or neutral direction.

very long-ranged and therefore highly susceptible to shear flow. In section IV we will discuss how this interaction affects the gas-liquid phase boundaries.

The phase behavior of non-spherical particles, in particular rod-like colloids, in shear flow is more complex. The phase behavior of colloidal rods in equilibrium is already very rich because two degrees of freedom play a role, namely positional and orientational ordering, while the anisotropy in the shape results in a cascade of positionally ordered states**, as described in chapter ?? on liquid crystals**. The effect of shear flow is most apparent in the orientational and positional disordered isotropic phase. Here, shear flow will perturb the orientation ordering of the system and will induce the formation of the orientational ordered but positional disordered nematic phase. The interaction between shear flow and the nematic phase, on the other hand, is very complex. In the last section V we will discuss how the different dynamic responses of the isotropic and nematic phase to shear flow affect the non-equilibrium phase behavior. We will start, however, by introducing the basic concepts of rheology, which are needed to understand the non-equilibrium phase behavior.

II. BASIC CONCEPTS OF RHEOLOGY

A. Definition of shear flow

The science of flowing materials is called rheology. In classical rheological experiments the force is measured that is required to strain a sample or,vice versa, the strain is measured which results from applying a force. The simplest and most applied deformation is the shear strain $\gamma = \frac{L}{h}$, when sample between two parallel walls is deformed by moving one wall relative to the other over a distance L in the x direction while both walls are a distance h apart in the y direction. For a small volume element this can be written as the gradient in the deformation field u_x, so that $\gamma = \frac{\partial u_x}{\partial y}$. A flow $\mathbf{v} = v\hat{x}$ will be induced when the sample is continuously strained. The flow rate depends on the distance from the moving wall y so that a shear rate can be defined as $\dot{\gamma} = \frac{\partial v_x}{\partial y}$. Thus the y-direction is called the gradient direction. The third direction is unperturbed and is called the neutral direction, or also the vorticity direction since it is set by $\nabla \times \mathbf{v}$. The different directions are schematically shown in Fig. 1.

The deformation rate tensor $\mathbf{\Gamma}$ describes the rate of deformation in 3 dimensions. For simple shear flow it reads

$$\mathbf{\Gamma} = \dot{\gamma}\hat{\mathbf{\Gamma}} = = \dot{\gamma}\begin{pmatrix} 0 & 1 & 0 \\ 0 & 0 & 0 \\ 0 & 0 & 0 \end{pmatrix}. \tag{1}$$

The most easily measurable force in rheology is generally the force that is exerted by the sample on the plane of the moving wall that is moving in the 1 ($= x$) direction, which has the normal parallel to the gradient in the flow which is the 2 ($= y$) direction. This stress is called the shear stress and is denoted by σ_{12}, where the indices refer to the plane on which the force is exerted (1) and the direction in which the force acts (2). σ_{12} is mostly referred to as the stress σ (or also often τ). Stresses in other directions are also important, especially for complex systems, but are often difficult to measure.

When the shear stress is proportional to the strain γ then the sample behaves like a solid and the proportionality constant G is the modulus, as introduced by Hooke:

$$\sigma_{12} = G\gamma. \tag{2}$$

When the shear stress is proportional to the rate of deformation $\dot{\gamma}$ then the sample behaves like a fluid and the proportionality constant η is the viscosity, as introduced by Newton:

$$\sigma_{12} = \eta\dot{\gamma}. \tag{3}$$

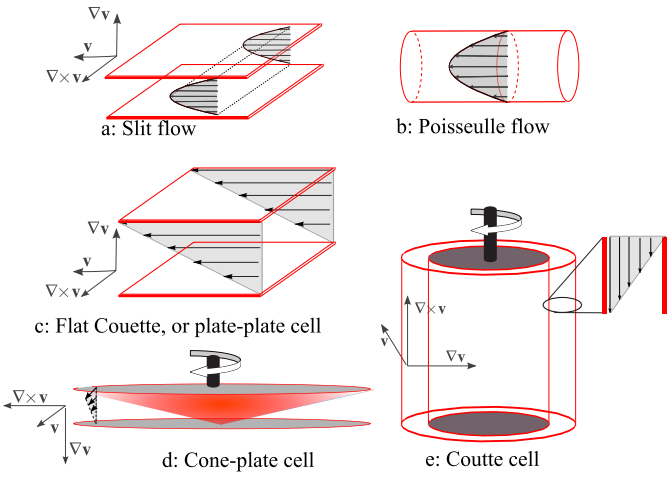

Figure 2: Shear geometries.

Often a material is not a solid and not a liquid, but something in between. These so called visco-elastic materials are best characterized by subjecting them to an oscillatory shear flow given by a time-dependent strain of

$$\gamma(t) = \gamma_0 \sin(\omega t). \tag{4}$$

This is the so called dynamic test. When the strain amplitude γ_0 is not too high so the sample does not change its character, then the response can be written as

$$\sigma_{12}(t) = G^* \gamma_0 \sin(\omega t + \delta) = [G' \sin(\omega t) + G'' \cos(\omega t)]\gamma_0. \tag{5}$$

The sample can thus be characterized by the modulus G^* and the phase angle, or by the storage modulus G' and loss modulus G''**see chapter ...**. The system behaves like a solid when $G' \gg G''$ and $\delta = 0^o$, and like a fluid when $G' \ll G''$ and $\delta = 90^o$. The system is visco-elastic when $G' \approx G''$ or $0 < \delta < 90^o$. Thus, rheology is an often used to probe the state of a material.

Standard geometries that are used to impose shear flow are depicted in Figure 2. The geometries can be categorized in pressure flow, where shear is generated by pushing sample through a channel, and drag flows, where shear is generated between a moving and a fixed wall. The choice of the geometry depends on many different aspects. For details on the advantages and disadvantages of the different shear geometries from a pure rheological point of few, please refer to Chapter 5 of Ref. [8].

Pressure-drop flow is often used for imaging, basically because it is very easy to set up. As can be appreciated from Fig. 2a-b, shear flow is parabolic throughout the cell, but will be linear close to the wall. In general, however, drag geometries allow for a better control over the shear and the shear rate is more (or less, see Ref. [8]) homogeneous. In the coming paragraphs we will refer to these geometries when discussing experiments.

While for a decent dynamic test care needs to be taken that the material is not influenced by shear flow, in this chapter we are interested in exactly that: how is phase behavior influenced by shear flow? Although there are rheological signatures for shear induced phase transitions, the interpretation is often ambiguous. Therefore it is important that the structure of the suspensions can be probed while shearing. This is an important factor that also determines the choice of the shear geometry, since in practice it is difficult to obtain reliable rheological and structural data simultaneously.

B. Scaling the shear rate

The implicit assumption in Newton's law for fluids is that the fluid behaves like a continuum which can be described by a single friction coefficient, namely the viscosity η. The continuum does not change its properties when subjected to shear flow because shear flow does not effect the particles constituting the fluid. To satisfy this condition, the memory of the fluid should be very short compared to the applied deformation rate. Thus, the relevant relaxation time of the system τ needs to be defined in order to estimate the effect of shear flow. This is expressed by the Péclet

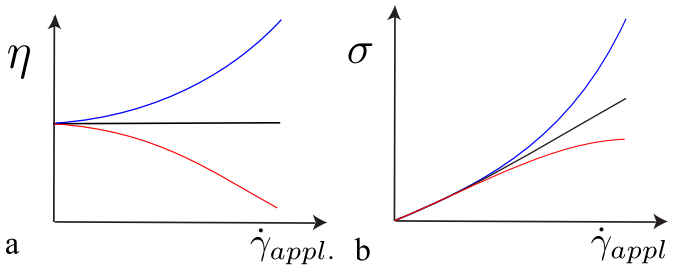

Figure 3: Cartoon of three different flow curves in viscosity vs shear rate representation and stress vs shear rate representation: Newtonian (black); shear thinning (red); shear thickening (blue).

number, which measures the shear rate relative to the respective relaxation process. This resulting scaled shear rate is called the Péclet number and is defined as $Pe = \dot{\gamma}\tau$. Similarly, the frequency in case of a dynamic test can be scaled, which is then called the Deborah number $De = \omega\tau$. Changes in the intermolecular structure of the solvent molecules are very quickly lost for simple fluids due to the diffusion of the molecules so that the relaxation time is very fast and $Pe << 1$. The diffusion rate D for colloidal spheres is

$$D_0 = k_B T/6\pi\eta R\,, \tag{6}$$

where $k_B$is Boltzmann's constant, R is the radius of the particle and η is the viscosity. Thus the time for a particle to diffuse its own diameter is $\tau = 1/R^2 D = 6\pi\eta R^3/k_B T$. In order for the shear rate to take effect it has to be of the same time scale so $Pe = \tau\dot{\gamma} = (6\eta\dot{\gamma})/\langle k_B T/R^3\rangle \approx 1$. For a colloid of $R = 500\ nm$ in water this means that a shear rate of $0.6\ s^{-1}$ is sufficient to compete with Brownian motion. When considering colloidal rods, shear flow will compete with the rotational motion of the rods. For slender rods of $1\ \mu m$ the rotational diffusion in water at room temperature is $D_R = 0.062\ s^{-1}$. So in order to have an appreciable alignment a shear rate of $\dot{\gamma} > \mathcal{O}(10\ s^{-1})$ needs to be applied.

So far we considered the shear rate needed to compete with Brownian motion. Often, however, particles interact with each other and form structures. Interactions generally slow down the dynamics, so that shear rate now needs to be scaled by the dynamics of the structure in order to appreciate the effect of shear on the structure and as a result on the phase behavior. In the remaining of this chapter we give a few insightful examples of how shear flow and structure are coupled.

C. Flow instabilities

As we mentioned earlier, for simple fluids the stress is proportional to the applied shear rate. But the colloidal dispersions that are discussed in this chapter, as well as many other materials, are not simple fluids and behave "'non-Newtonian"'. The reason for this was just discussed above: if the shear rate is faster than the dynamics in the system then the system will be perturbed by the shear rate and change its properties. The direct consequence will be that the viscosity of the sample will change with the shear rate that is applied. This will be apparent when taking a flow curve where the stress, and hence the viscosity, is measured as a function of shear rate.

The simplest flow curve is a straight line where the viscosity does not change with shear rate or the stress increases linearly. The main other examples are a shear thinning flow behavior, where the viscosity decreases with increasing shear rate, and a shear thickening flow behavior where the viscosity increases with increasing shear rate, as shown in Fig. 3. Strong shear thinning is a very desirable feature for industrial applications. The flow behavior of shampoo, for example, is mainly engineered by using surfactant wormlike micelles: at low shear it behaves like a gel, at high shear it flows very easily. The same features are also very useful in, e.g. the oil industry [9]. Shear thickening is used for dampening materials like body armour. When a bullet enters a jacket with shear thickening material at high speed then this material stiffens and the bullet is slowed down [10].

When the flow behavior is extremely non-Newtonian then the stress behavior can cause mechanical instabilities in the shear cell. This means that instead of a smooth linear flow profile between the moving wall and the standing wall, as is required for Newtonian flow, the flow will be structured: regular or irregular (turbulent) flow profiles will develop in either the vorticity direction, the gradient direction or both.

Flow instabilities can be predicted on the base of constitutive models that describe shear thickening and thinning behavior. Constitutive models that describe extreme shear thickening assume a functional form as depicted in Fig. 4a, where the dashed line represents meta- or unstable states. A stable state, assuming laminar flow, would be achieved

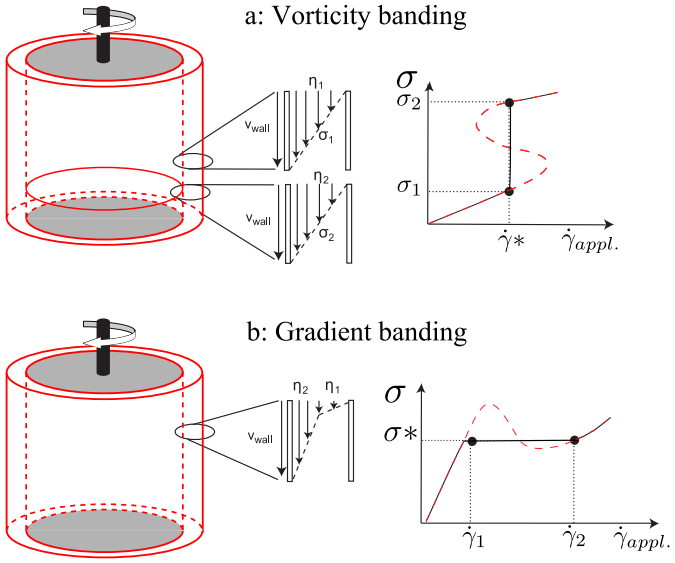

Figure 4: Two types of shear banding: in the vorticity direction (a) and in the gradient direction (b). The flow profiles are indicated in the middle by the different lengths of the arrows. To the right flow curves underlying the shear band formation at the right.

when alternating bands are formed with different viscosity, stacked along the vorticity direction [11]. The bands have a different stress since they are subjected to the same shear rate, as indicated by the dotted lines in the right panel of Fig. 4a. This "classical" picture of vorticity banding is shown schematically on the right of Fig. 4a. The question is, however, what mechanism drives the formation of these bands and whether the flow within the bands is laminar with equal shear rates.

Constitutive models that describe extreme shear thinning again assume a functional form as given in Fig. 4b, where again the dashed line represents meta- or unstable states: the part where the stress decreases with increasing shear rate renders the system mechanically unstable. "Unstable" means in this case that small deviations from the linear velocity profile will grow. From a theoretical point of view this is very similar to an equilibrium gas-liquid phase separation [12, 13], as will be discussed in section IV. In the 'classical' picture of gradient band formation, at the end of the shear driven phase separation, the system splits up into a region of a low viscosity and high shear rate close to the moving wall and a region with a high viscosity and low shear rate close to the static wall such that the stress in both bands is constant, see the left of Fig. 4b.

Gradient banding in shear flow is far better documented [14] and understood [15, 16] than vorticity banding. In principle its occurrence is independent of the structural changes in the fluid underlying the shear thinning behavior, as long as the shear thinning is substantial. Thus gradient banding has been observed for systems ranging from hard sphere colloidal crystals [17] and soft colloidal glasses [18] to associative polymer networks [19], entangled polymer solutions [20, 21] and DNA solutions [22, 23]. Shear thinning behavior is far more pronounced for dispersions of living polymers, which consist of monomers that continuously break and recombine. This class of polymers has two mechanisms to release stress: reptation and the break up and recombination of the polymers. For the case where the average breaking time is much faster than the reptation time it can be shown that this results in a unique relaxation mechanism and strong shear thinning [24, 25]. Surfactant wormlike micelles are self-assembled particles, and display strong shear thinning, which is easily tunable [26, 27]. Therefore wormlike micelles are the 'working horse' for experimentalists in the field of flow instabilities. The first experimental proof for the occurrence of structure formation in the fluid were birefringence measurements showing the split up of fluid into regions with low and high birefringence, i.e. probably into regions with high and low viscosity respectively [28]. This strongly suggests that the shear rate in the two regions is different. The existence of shear banding in this class of systems has first been shown by Callaghan et al. in a pipe-flow geometry using Nuclear Magnetic Resonance Microscopy [29]. Using Heterodyne Dynamic Light Scattering Salmon et al [30] demonstrated for the first time that indeed a scenario is at hand where the systems splits up in two bands with shear rates of $\dot{\gamma}_1$ and $\dot{\gamma}_2$ using the couette geometry. The contribution of both bands is set by the lever rule, similar to the lever rule for gas-liquid phase separation. The mechanisms of shear band formation and the relation with the birefringent structures was nicely demonstrated both by Hu and Lips [31] and Miller and Rothstein [32]. Both groups used Particle Imaging Velocimetry (PIV) in combination with small angle light scattering and birefringence imaging. Even more structural insight was supplied by using a combination of small

angle neutron scattering and shear flow [33].

Vorticity banding is less common than gradient banding. A detailed recent discussion of elastic instabilities that drive the formation of vorticity bands can be found in Ref. [34]. The classical picture of vorticity banding due to shear thickening is more the exception than the rule, although again for wormlike micelles the predicted behavior has been found [35]. Another, more common, mechanism is that normal stresses are generated through the non-linear elastic deformation of the dispersed mesoscopic entities, similar to the Weissenberg effect in polymeric systems [36]. The role of the polymer chains in the classic Weissenberg effect is now played by large scale networks, such as carbon nanotube dispersion [37] and clay gels[38], or inhomogeneities formed during the initial stages of phase separation as found for polymer-protein mixtures [39] and coexisting colloidal [40]. These structures will be non-uniformly stretched due to the curved streamlines that are present in most rheological devices, thus generating hoop-stresses that give rise to elastic normal forces [41]. Another mechanism for the formation of vorticity bands shear bands connects gradient and vorticity banding. There is experimental evidence [42, 43] and theoretical justification [44] that vorticity bands are formed due to instabilities in the interface between two gradient bands. All of these scenarios lead to rolling motion within the bands, superimposed on the laminar flow. This rolling motion is absent in the classic picture, depicted in Fig. 4a. Note also that these are a pure elastic instabilities and that inertia does not play a role as is the case for well known Taylor instability [45].

III. EFFECT OF SHEAR FLOW ON CRYSTALLIZATION OF COLLOIDAL SPHERES

Colloidal particles with the simples interaction potential and the simplest shape are colloidal hard spheres. Despite of this conceptual simplicity it is impossible to calculate the phase diagram with analytic theories. It was only in 1957 that one of the first computer simulations were used to show that hard spheres undergo a transition from a liquid phase, where particles can be at any position in space, to a solid phase, where the particles are bound to their crystal lattice positions [46]. Since hard spheres have no potential energy, their phase behavior is determined entirely by entropy and depends only on volume fraction φ [47]. These system can still order, and thus reduce the entropy, because locally the particles will have more free volume, thus increasing the entropy. Fluid and crystal coexist between the freezing point $\varphi_f = 0.494$ and the melting point $\varphi_m = 0.545$, while pure crystal is stable for $\varphi > \varphi_m$, as shown again by simulations [48]. The volume fractions that boarder the phase coexisting region areφ_f and φ_m are called the binodal points. Colloidal systems proved to be ideal to study these most fundamental transitions, once chemist were able to synthesize particles that behave almost like billiard balls. The complete phase diagram was experimentally determined using dispersions of polymer coated polymethylmethacrylate particles, including a transition to a glassy state of random close packed spheres at even higher concentrations [49]. Nonetheless, colloids will always have some softness, albeit due to the repulsive polymer layer that is grafted on their surface or due to the surface charge. For extremely charged colloids it was even possible to make crystals with up to 1 % of the volume occupied by particles [50]. Scaling of the volume fraction is thus performed by using an effective diameter. The other appeal of colloidal spheres is that they allow for direct visualization of one of the most fundamental processes of structure formation [51] which allows comparison with simulations [52]. A nice overview on crystallizing colloids is given in Ref. [53].

We will discuss here the effect that shear flow has on the liquid-crystal phase transition. The flow behavior of colloid hard sphere dispersions in the liquid phase is a very extended field of research, both for practical and fundamental reasons.While at low concentrations the viscosity is merely increasing [54], colloidal dispersions attain a highly non-linear visco-elastic behavior at high concentrations, approaching the liquid-crystal transition. This is due to the fact that the shear induced distortion on the particle level, leading to extreme shear thickening behavior [55]. Shear flow per definition affects the crystal structure because particles are displaced from their fixed lattice positions. Thus the rate of deformation competes with the rate that crystals are formed. In this way the effect of shear flow is connected to the kinetics of the phase transition, so how do the crystals form without flow. As we will see, there is a cascade of different states into which the quiescent crystal can be transformed, while crystallization of a quiescent amorphous dispersion can also be induced by shear flow. We will discuss two types of non-equilibrium phase diagrams. First the effect of oscillatory shear flow on the structure and phase behavior is discussed and then the effect of steady shear flow. The transition between the different states will show to have a pronounced influence on the flow behavior of these highly structures dispersions. The sequence of transitions and the phase which will be described below are neither complete nor universal. Subtle changes in the particle interaction can already alter the shear response. The aim is, however, to convey an idea about the physical processes at hand. For an overview on the structure of colloidal spheres in shear flow we refer to Ref. [56].

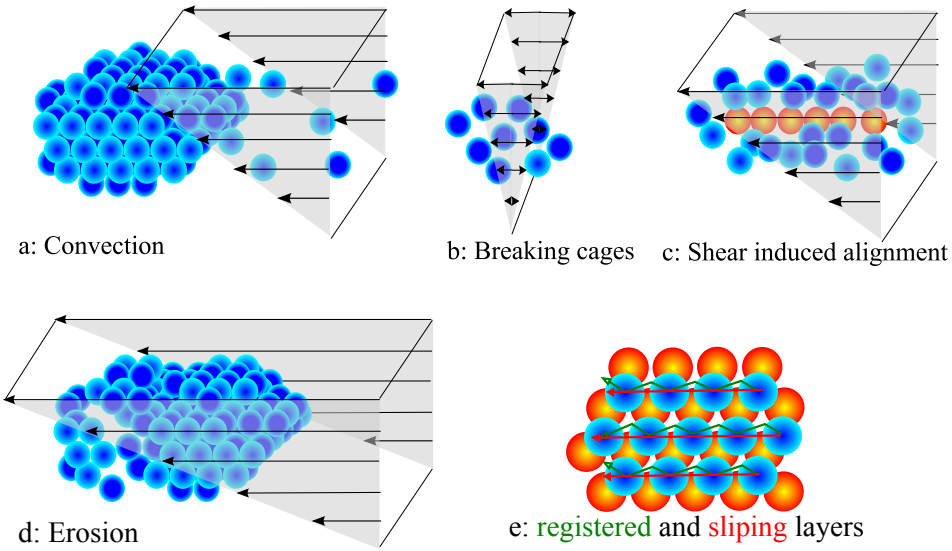

Figure 5: Sheared colloidal crystal: positive effects due (a) to convection of particles to nucleus, (b) cage braking, and (c) alignment of spheres; negative effects due to erosion (d) and registered motion (e).

A. Equilibrium phase behavior

According to *Classical Nucleation Theory* (CNT, see [57] for a review) the kinetics of crystallization is determined by two processes. First a crystal nucleus needs to be formed out of the isotropic background. This is a process with an activation energy barrier and therefore it has an induction time τ_{ind}. The activation barrier is due to the balance between the energy penalty for the formation of a sharp interface and the energy gain due to the formation of the new phase with lower free energy. The decrease in the bulk energy depends on the difference between the solid and liquid chemical potentials $\Delta\mu$ times the volume of the newly formed nucleus, while the increase in surface energy depends on the solid-liquid interfacial tension γ times surface of the nucleus. Both contributions result in a free energy barrier $\Delta G_{\rm crit}$ for the formation of a nucleus

$$\Delta G_{\rm crit} = \frac{16\pi}{3}\gamma^3/(\rho_s\Delta\mu)^2)\,, \tag{7}$$

where ρ_s is the number-density of the solid.

The rate I at which nuclei are formed depends exponentially on $\Delta G_{\rm crit}$ and on the second process of crystallization, namely the rate at which particles diffuse to the formed nucleus, given by the kinetic factor κ, which is connected to the short-time self-diffusion constant of the colloids. I can now be written as

$$I_{growth} = \kappa \exp -\Delta G_{\rm crit}/k_BT\,, \tag{8}$$

where T is the absolute temperature, k_B is Boltzmann's constant. Eq. (8) contains the functional dependence of the nucleation rate on the relevant physical quantities $\Delta\mu$, κ and γ. *A priori* knowledge of these quantities is needed to make quantitative predictions of the nucleation rate. Since to date there is no theory that provides 'first principles' predictions of these parameters, estimates need to be made depending on the exact system. For hard spheres it is predicted that the nucleation rate displays a maximum as a function of the volume fraction: while the driving force $\Delta\mu$ increases with increasing concentration, the diffusion slows down until it is arrested at the glass transition [58]. The slowing down is less dramatic for charged spheres and therefore no maximum is expected. The general trend was confirmed by a vast amount of light scattering experiments [59–61]. Experiments and simulations can be compared after performing a careful scaling of the experimental volume fraction, as described above. A reasonable agreement is found at high concentrations, but the nucleation rate found in simulations at low volume fractions approaching the freezing point φ_f are several orders of magnitude slower. The exact reason for this discrepancy is not yet known.

B. Non-equilibrium phase behavior

There are many ways how shear flow can perturb the crystallization process, as depicted in Fig. 5. Shear flow can *enhance* the growth rate by convecting particles to the crystal nucleus, as shown in Fig. 5a. Another way how shear flow enhances mobility is by braking cages which form at high concentrations, as shown in Fig. 5b. This is specially of importance for hard spheres, which have the tendency to jam into a glassy state. In both cases the diffusion of the constituents is enhanced so that the diffusive term κ in Eq. (8) is replaced by a convective shear dependant term. Finally, shear flow can also induce ordering by aligning spheres into strings. This potentially plays a role in decreasing the energy barrier $\Delta G_{\rm crit}$ since it creates already an interface, as shown in Fig. 5c. On the other hand shear flow can also *frustrate* crystallization and/or destroy crystals. First, when a sample is crystallizing but not yet fully crystalline then the surface of the crystal nuclei can be eroded by the shear flow, as shown in Fig. 5d. Second, when fully crystalline samples are subjected to shear flow then the crystal will have to deform by the shear and finally yield. This effect is dramatic when the crystallite has the wrong orientation with respect to the shear flow which will readily cause the destruction of the crystallite by shear. Sheared crystals will therefore only grow when they have the right orientation to accommodate deformations. In Fig. 5e there ae two mechanisms depicted that might take place. At low shear rates, when the system is given sufficient time, layers of crystals may slide over each other by a registered motion. Here the spheres jump between the points in the crystal lattice in a zig-zag motion. At high shear rates layers will slip over each other. This motion can only be accommodated when the crystal is somewhat deformable, so when the interaction potential between the particles is soft, or when the concentration is not too high.

The experimental signature of crystals is very clear when using scattering techniques, since Bragg diffraction from crystals cause strong scattering peaks. These peaks emerge out of a background diffuse "Debye-Scherrer" ring, characterizing the liquid structure factor. A hexagonal pattern will be observed when a sample consists of a single crystal. Samples will often be poly-crystalline so that scattering will take place from crystallites with many different orientations, resulting in a diffuse ring. Since the emergence of fluorescently labeled colloids in combination with confocal microscopy, real space measurements reveal details that are lost in ensemble averaged techniques like scattering. Very important are also macroscopic measurements, in particular rheological measurements, where for example the viscosity is measured as a function of shear rate. The above mentioned processes can thus be studied with this set of experimental tools.

Pioneering work on crystallization of colloidal hard spheres in shear flow is due to Bruce Ackerson and co-workers, employing the same grafted PMMA spheres as was used to determine the equilibrium phase diagram [49]. The main experimental technique that was applied was light and neutron scattering in combination with steady and oscillatory shear flow, as schematically shown in Fig. 6. Here, the incident radiation propagates along the centreline of the shear cell or along the tangent, probing the flow-vorticity and flow-gradient plane, respectively. In principle all possible effects that shear flow has on crystallization have been found by him and his co-workers. Their findings are summarized in a seminal paper in 1990 [62] and they will be discussed below.

The most subtle method of probing the effect of shear flow on crystallization is by applying oscillatory shear, see Eq. (4). In this way the effect of the strain deformation that is needed to aid (Fig. 5a-c) or frustrate crystallization (Fig. 5d,e) and time needed to take effect can be varied independently, although the frequency was fixed in the experiments discussed below. Oscillatory shear flow will induce crystallization at volume fractions as low as ($\varphi = 0.47$), for which the equilibrium sample is liquid-like ($\varphi < \varphi_f$), but only at sufficiently high strain amplitudes of $\gamma_0 > 1$. This means that both the Péclet number and the deformation need to be high enough. At strain amplitudes of $\gamma_0 > 2$ layer structure is observed and at even higher strain amplitudes the structure melts. For a volume fraction of $\varphi = 0.50$ phase coexistence is observed in equilibrium ($\varphi_f < \varphi < \varphi_m$) and the same transitions as described before, just at lower strain amplitudes. For ($\varphi = 0.553$) the sample is fully crystalline at equilibrium ($\varphi > \varphi_m$), while already small strain amplitudes force the system into a oriented Face Centered Cubic (fcc) crystal structure. At higher strain amplitudes the sample yields by forming layers that slide over each other. For a volume fraction of $\varphi = 0.595$ the equilibrium spheres are randomly closed packed in a glassy state. The glassy state and the liquid state as found for $\varphi = 0.47$ are structurally the same. Also for $\varphi = 0.595$ crystal formation is induced by shear. In this case shear induced crystallization is due to cage breaking as schematically shown in Fig. 5b, and not due to alignment of the spheres as in Fig. 5c, which is the mechanism expected for the concentrated liquid phase. At high strain amplitudes the system yields by forming layers that zig-zag over each other, since there is not enough space for sliding. A non-equilibrium phase diagram was thus obtained by varying the volume fraction of the colloids and the amplitude of the applied shear γ_0, as depicted in Fig. 7a.

Ackerson et al realized that different transitions between dynamical states are accompanied by different crystal structures. The transitions were interpreted by using models that describe what strain can be accommodated before particles bump into each other, which depends on the crystal structure [62]. These models can be best validated by observing the structures in real space. First attempts showed an intriguing shear-induced buckled state for an equilibrium fcc structure in confinement [64]. Later studies use a counter-rotating shear cell in combination with

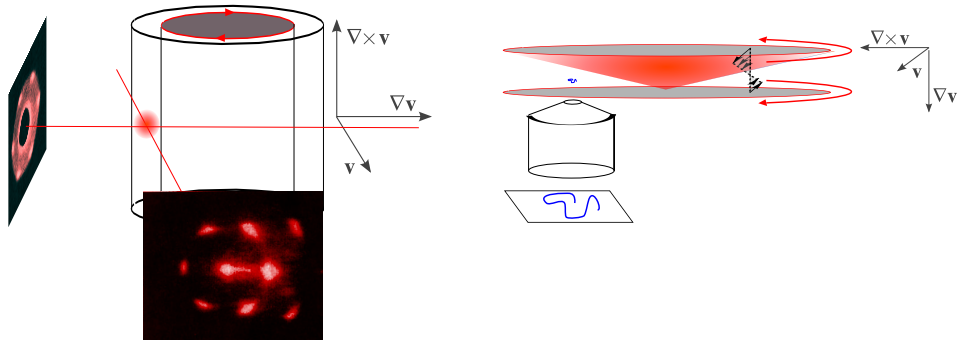

Figure 6: Geometries where sheared structures can be probed *in situ* using scattering (a) and confocal microscopy (b).

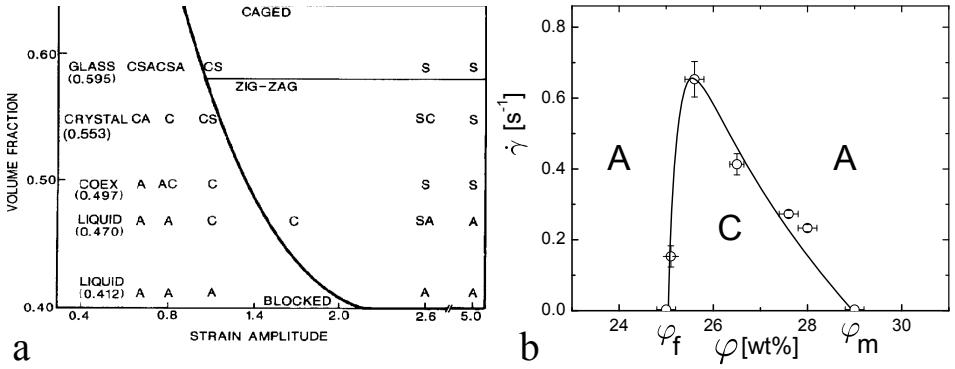

Figure 7: Non-equilibrium phase diagrams for crystallizing colloidal spheres. (a) Oscillatory shear phase diagram as a function of volume fraction of hard spheres and strain amplitude at 3.5 Hz. Reprinted with permission from Ref. [62]. Copyright 1990, The Society of Rheology. The symbols correspond to crystalline order (C), layer ordering (S), and amorphous order (A). The first symbol in a grouping indicates the predominant ordering observed. (b) Steady shear phase diagram as a function of volume fraction of charged spheres and shear rate. The symbols are the same as for (a). Adapted with permission from Ref. [63]. Copyright 2005 American Chemical Society.

confocal microscopy, as depicted in Fig. 6b, in which a stationary layer can be positioned away from the glass wall so that the particles stay in the field of view [65, 66]. With this technique the existence of the oscillating twinned fcc phase, the sliding layer phase and the shear induced strings have been confirmed. In addition, a state where the crystal makes an angle with the flow direction was found, while non-equilibrium Brownian dynamics simulations complied with the experimental findings [66].

Ackerson et al also studied the effect of steady shear flow on crystallization of colloidal spheres. They observed that layering is present at high concentrations and shear flow, but there is always evidence for the existence of an amorphous distorted structure. Only at low shear rates a transition is observed from a random close packed crystal to a flow oriented fcc. The same sequence of transitions was observed for crystals consisting of micelles of block-copolymers using Small Angle X-ray and Neutron scattering [67]. These systems are basically small colloidal spheres (radius of 12 nm) with soft interactions. The transitions were located at much higher shear rates, which is related to the small size and fast relaxation of the particles, see Eq. (6). The zig-zag motion was observed in real space using the counter-rotating shear cell in combination with a fast confocal microscope. This technique has the advantage that the local motion of the particles can be followed. As a consequence, it could be shown how the crystal shear melts when the particles have random displacements of more than 12% of the particle separation, reminiscent of the Lindemann criterion for melting in equilibrium systems [65].

These dynamic transitions underlay the non-equilibrium phase behavior of colloidal crystals in shear flow. To obtain the full phase diagram one needs to determine the shear rate dependence of the non-equilibrium binodal points $\varphi_f(\dot{\gamma})$ and $\varphi_m(\dot{\gamma})$. The best way to obtain these points is by monitoring the kinetics of the crystallization. In Ref. [63] the crystallization kinetics of charged silica spheres in shear flow was studied. This system freezes at a volume fraction as low as $\varphi_f = 0.25$ while at $\varphi = 0.29$ it forms an amorphous glass [68]. The advantage of charged systems is that the crystals are much softer and form faster. Shear flow can be conveniently used to create a melted initial state

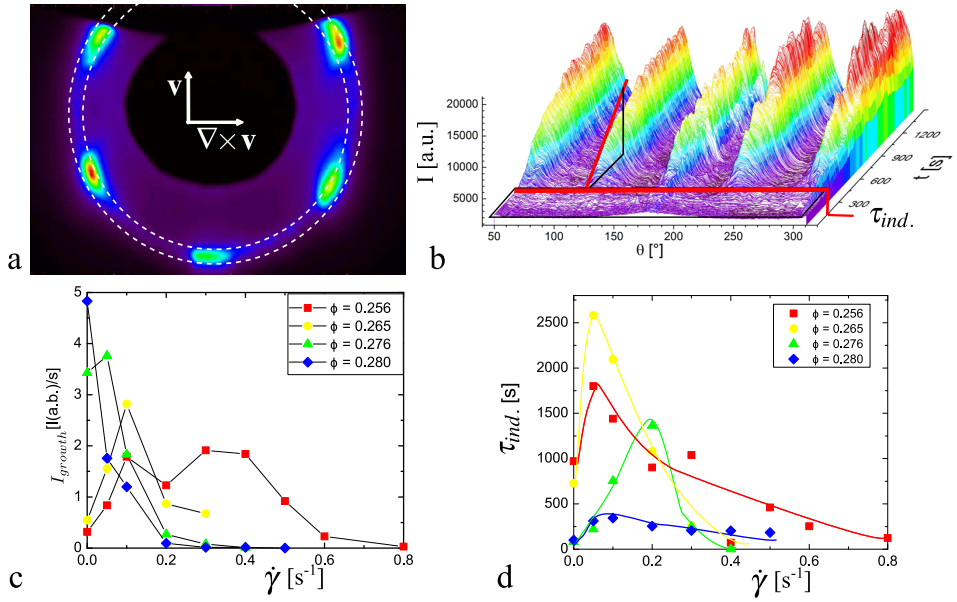

Figure 8: Crystallization kinetics of charged colloidal spheres after a quench from a high shear rate where the crystal structure is melted to a final shear rate. (a) Light scattering pattern using a geometry as in Fig. 6a, probing the flow-vorticity plane. The pattern is taken 1500 seconds after a quench to a shear rate of 0.05 s^{-1}. (b) Azimuthal profiles taken at the scatter angle of the first order Bragg peaks, dashed lines in (a), as a function of time after the quench to $\dot{\gamma} = 0.05\ s^{-1}$. The growth rate I_{growth} is obtained from the slope of the red line and and induction time τ_{ind} is obtained from the start of growth. τ_{ind} and I_{growth} are plotted in (c) and (d), respectively, as a function shear rate φ for various volume fractions. The figures are adapted with permission from Ref. [63]. Copyright 2005 American Chemical Society.

using a high shear rate, followed by a quench at $t = 0$ to the shear rate for which the crystallization will be studied. Fig. 8a displays a typical scatter pattern as formed 1500 seconds after a quench to a shear rate of 0.05 s^{-1}, showing clear Bragg peaks of an oriented crystal. The kinetics of the formation of this structure is most conveniently followed when plotting the azimuthal profile taken at the peak position, see Fig. 8b. The nucleation time τ_{ind} and growth rate I_{growth} can be obtained from the evolution of the azimuthal profile: the growth rate relates to the slope of the total intensity as a function of time and the induction time is obtained from the crossing of this slope with the background, see Fig. 8b. The thus obtained induction times τ_{ind} and growth rates are plotted in Fig. 8c and d, respectively, as a function of shear rate for various concentrations. The phase boundary at low concentration is determined from these plots by extrapolation to the concentration where where the inverse of induction time τ_{ind} goes to zero ($1/\tau_{ind} \to 0$), while the boundary at high concentration and shear rate is found by extrapolation to the point where the growth rate goes to zero ($I_{growth} \to 0$).

The resulting non-equilibrium phase diagram of sheared charged colloids, as plotted in Fig.7b, is strongly peaked due the competing effects of shear flow. The phase boundary at low concentration is almost vertical and therefore independent of the shear rate. This implies that at low concentrations the chemical potential difference $\Delta\mu$ and interfacial tension γ between the liquid and crystal, see Eq. (7), are almost independent of the shear rate. Indeed at low concentration the induction time τ_{ind} is not very sensitive to changes in the shear rate, see red curve in Fig. 8. For higher concentrations the induction time exhibits a maximum as a function of the shear rate. The increase in τ_{ind} with increasing shear rate for the lower rates is probably connected to the suppression of nuclei formation, as found in simulations [69]. The decrease of τ_{ind} at higher shear rates is probably related to shear induced alignment of the spheres, lowering the surface tension γ. Without shear flow τ_{ind} decreases with increasing concentration, which complies with a decrease in the energy barrier. The growth rate without shear flow increases monotonically as a function of concentration, which complies with an increased concentration of spheres and therefore of Δmu, see Eq. (8). The fact that the growth rate displays a maximum at low concentrations as a function of shear rate nicely illustrates the competing effects of shear flow. Low shear rates enhance transport of particles towards the nucleus, as illustrated in Fig. 5a, and therefore the kinetic factor κ, while at high shear rates erosion takes place, as in Fig. 5d. For higher concentrations there are more particles available for the crystallite so that shear flow only erodes the crystallites, as illustrated by the monotonous decay of the growth rate as a function of shear rate.

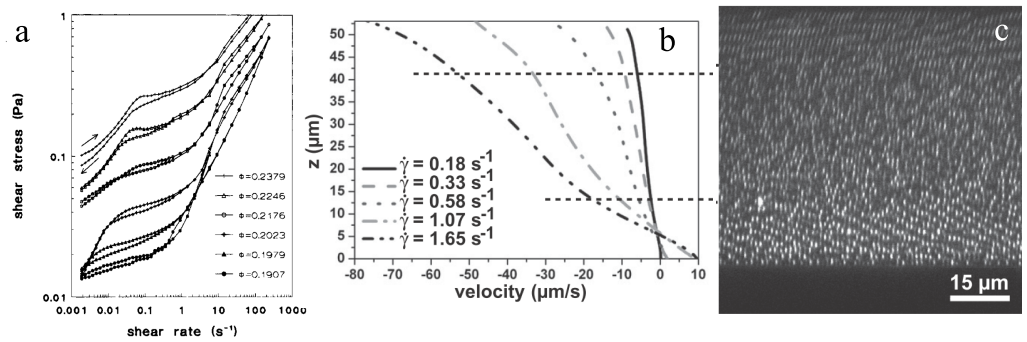

Figure 9: (a) Flow curves for charged silica spheres at different volume fractions showing strong shear thinning when increasing the shear rate. Reprinted (adapted) with permission from Ref. [17]. Copyright 1994 American Chemical Society. (b,c) Shear banding in colloidal crystals observed with *In situ* confocal microscopy measurements, using a cone-plate shear cell as depicted in Fig. 6b. Reprinted from Ref. [74]. (b) Flow profiles of a $\varphi = 0.50$ dispersion of silica particles measured for various applied shear rates. The local shear rate was significantly higher at both the top and bottom plate. (c) Confocal microscopy image of the velocity-gradient plane taken immediately after cessation of the flow, using a cone-plate geometry as shown in Fig.6b. At both walls, the particles arranged in crystalline layers, but in the middle, the structure was liquid like. Horizontal dashed lines indicate these boundaries and show the correspondence with the flow profiles.

C. The effect on flow behavior

We have so far described a number of structural changes that can be induced by shear flow, either creating or destroying crystals. These changes are accompanied by changes in the mechanical properties of the systems. Indeed dynamic rheological tests show that the modulus G^* around the crystallization point is lower in the crystal phase than in the liquid phase, while in both phases storage modulus G' is higher than the loss modulus G'' [70], indicating a transition between two solid states.

Steady shear experiments show that the softening of the material is also apparent from the strong shear thinning which has been seen for a variety of systems [17, 71, 72]. Example of a flow curve which exhibits shear thinning is shown in Fig. 9a for a system of charged spheres at various concentrations. For all of these systems the shear thinning is accompanied by the formation of regions where the sample is crystalline and regions where the sample is amorphous. As explained in section II C, it is expected that a strong shear thinning system will form shear bands with different shear rates. With the development of *in situ* confocal microscopy it is possible to determine the structure at the same time as the flow profile. For both oscillatory [73] and steady shear flow it was observed that the high shear rate and low viscosity region is the crystalline region; the low shear rate and high viscosity region has an amorphous structure [74], see Fig. 9b,c.

The occurrence of such a pronounced flow behavior depends on many factors. If the spheres are very charged, as the system used in section III B, then the interaction between the spheres is so soft that the stress barrier for the formation of structurally different sample is low. The history of the sample is important as can be deduced from the fact that the flow curve obtained by increasing the shear rate is different from the flow curve obtained by decreasing the shear rate, see Fig. 9a. This also shows that the flow behavior depends on the initial condition of the sample, which could be a poly-domain crystal, amorphous or pure crystal etc. Although all these subtleties are very important, for now it is sufficient to realize that indeed the macroscopic flow behavior is set by the formation and destruction of crystalline microstructure.

IV. EFFECT OF SHEAR FLOW ON GAS-LIQUID PHASE SEPARATING COLLOIDAL SPHERES

The phase behavior of particles with an attractive interaction potential is very different from repulsive or hard spheres and therefore also the effect of shear flow is expected to be very different. **Chapter ...** describes the different effects that attraction can have, focusing on gelation, which typically occurs when particles have a short ranged and deep interaction potential. Moderate attractions cause the system to separate in a phase with low density, the gas phase, and a phase with high density, the liquid phase. The gas-liquid phase separation of colloids is very similar to the molecular gas-liquid phase separation, but also to binary liquids and polymer solutions. All of these classes of systems have a critical point, where the binodal and spinodal lines meet.

The spinodal line separates the meta-stable region from the unstable region in the phase diagram. Within the unstable region, an initially homogeneous system evolves continuously towards the demixed state. In contrast, the

binodal separates the stable from the meta-stable region of the phase diagram. Demixing from the meta-stable region evolves through nucleation-and-growth, where on formation of the nucleus a discontinuous jump to a locally relatively high concentration occurs, as we saw for crystallization. At the spinodal, the (effective) diffusion coefficient D_{eff} vanishes, which is commonly referred to as "critical slowing down". Slowing down of dynamics at the spinodal is due to a cancellation of the Brownian forces (which tend to homogenize the system) and the attractive interactions between the colloidal particles (which favor demixing). The driving net force for colloidal-particle displacements is thus very small, leading to very slow dynamics. In addition, the range of interactions between two colloidal particles as mediated through many intermediate colloids diverges at the spinodal. The divergence of this interaction range, the so-called correlation length ξ, was first described by Ornstein and Zernike [75]. Both of these effects are quantified by a vanishing concentration derivative of the osmotic pressure, as will be discussed later. Whereas the effective diffusion coefficient is zero at the spinodal, it becomes negative on crossing the spinodal into the unstable region, which mathematically describes the continuous growth of inhomogeneities. The initial stage of spinodal decomposition is thermo-dynamically described for the first time in Ref. [76], which theory is now known as the Cahn-Hilliard theory.

Due to the very slow dynamics near the spinodal, unusually small shear rates are sufficient to significantly distort microstructural order. This is mathematically quantified by an effective Peclet number which contains both the effective diffusion coefficient and the correlation length, as will be seen later. Onuki discussed a description of the effect of shear on critical systems, using a renormalization group approach. It was shown that phase separation is suppressed by the effect that shear flow has on the life time of concentration fluctuations [77]. Experiments on semi-dilute polymers solutions revealed that shear flow can also enhance concentration fluctuations, which induces phase separation [78]. This is in accordance with dynamic theories where shear-induced stresses generated by internal degrees of freedom and entanglements of the polymers were implicitly included. It was shown that the spinodal is suppressed in the vorticity direction and enhanced in the gradient direction [79, 80]. These theories are to some extend applicable to colloidal dispersions [81]. A nice review of the critical behavior in shear flow is given by Ref. [82].

We focus in this chapter on the phase behavior of colloids in shear flow, so that the interest here is in the development of a non-equilibrium theory for concentrated colloidal systems with attractive inter-colloidal interactions. The way to progress is by using microscopic theories that describe the distribution of positions for individual particles and how this distribution evolves in time. In other words, an equation of motion for the probability density function of the particle positions needs to be developed. This type of theory has the advantage that it is straightforward to incorporate shear flow, which is (at least in principle) not possible through a quasi-thermodynamic approach as shear flow is a non-conservative external field. The equation of motion for the position coordinates of an assembly of many colloidal particles is the so-called Smoluchowski equation. In the following we will first describe how critical slowing down (quantified through the effective diffusion coefficient D_{eff}) and the divergent correlation length ξ can be obtained from the Smoluchowski equation for attractive colloidal spheres without shear flow and then how these parameters are affected by shear flow. Details of this theory can be found in Refs. [54, 83–85]. This theory will be contrasted to light scattering experiments. We will finish this section, describing the effect of shear flow on demixing systems and see how this affects the stability of the system.

A. Equilibrium phase behavior

The Smoluchowski equation of motion for the probability density function $P \equiv P(\mathbf{r}_1, \mathbf{r}_2, \cdots, \mathbf{r}_N, t)$ of the position coordinates $\mathbf{r}_j$, $j = 1, 2, \cdots, N$, of all N colloidal particles in the system reads, with the neglect of hydrodynamic interaction, is given by

$$\frac{\partial}{\partial t} P \;=\; D_0 \sum_{j=1}^{N} \nabla_{r_j} \cdot \left[\beta [\nabla_{r_j} \Phi] \, P + \nabla_{r_j} P \right] . \tag{9}$$

Eq. (9) relates the probability of finding a particle in a certain volume to the forces acting on it, either mediated by the other particles, fist term on the right, or by the randomizing Brownian diffusive forces, second term on the right. Here D_0 is the Stokes-Einstein diffusion coefficient, $\beta = 1/k_B T$ (with k_B Boltzmann's constant and T the temperature). $\Phi \equiv \Phi(\mathbf{r}_1, \mathbf{r}_2, \cdots, \mathbf{r}_N)$ the potential energy of the assembly of colloidal particles.

In order to predict if a system is stable one needs to check if the average distance between the particles is stable. The correlation between the relative position of two particles is described by the pair-correlation function $g(t)$ which is defined as

$$\begin{aligned} P_2(\mathbf{r}_1, \mathbf{r}_2, t) \;&\equiv\; \int d\mathbf{r}_3 \cdots \int d\mathbf{r}_N \, P(\mathbf{r}_1, \mathbf{r}_2, \mathbf{r}_3, \cdots, \mathbf{r}_N, t) \\ &\equiv\; P_1(\mathbf{r}_1, t) \, P_1(\mathbf{r}_2, t) \, g(\mathbf{r}_1, \mathbf{r}_2, t) \, . \end{aligned} \tag{10}$$

Note that the reduced pdf for a single particle P_1 is per definition $P_1 = 1/V = \rho/N$ (where V is the volume of the system, N the total number of spherical colloids, and $\rho = N/V$ the number density). The potential is taken equal as a pairwise of so called pair-interaction potentials $V(r_{ij}$, that is (with $r_{ij} = \mid \mathbf{r}_i - \mathbf{r}_j \mid$),

$$\Phi(\mathbf{r}_1, \mathbf{r}_2, \cdots, \mathbf{r}_N) \; = \sum_{i,\, j \,=\, 1 \,,\; i \,<\, j}^{N} V(r_{ij}) \, . \tag{11}$$

This is the point where the attraction between particles comes into play. Integration of the Smoluchowski equation (9) gives (with $\mathbf{R} = \mathbf{r}_1 - \mathbf{r}_2$ the distance between two spherical colloids and ∇ the gradient operator with respect to $\mathbf{R}$),

$$\frac{\partial}{\partial t} \, g(\mathbf{R}) \; = \; 2 \, D_0 \nabla \cdot \left\{ \, \nabla g(\mathbf{R}) + \beta \, g(\mathbf{R}) \left[\, \nabla V(R) - \mathbf{F}^{ind}(\mathbf{R}) \, \right] \right\} \, . \tag{12}$$

Here, $\mathbf{F}^{ind}$ is the "*indirect force*" between two particles, which is mediated via a third particle, and is equal to

$$\mathbf{F}^{ind}(\mathbf{R}) \; = \; -\rho \int d\mathbf{r} \, [\nabla V(r)] \, \frac{g_3(\mathbf{r}, \mathbf{R})}{g(\mathbf{R})} \, , \tag{13}$$

where $\rho = N/V$ is the particle number density and $g_3(\mathbf{r}, \mathbf{R})$ is the three-particle correlation function; $\mathbf{r}$ is the distance between particle 1 and a third particle, $\mathbf{r} = \mathbf{r}_1 - \mathbf{r}_3$.

For critical phenomena the indirect force is essential, being responsible for the long ranged interactions between two spheres as mediated through the remaining spheres. Thus, we want to find a solution for Eq. (12) for distances $R \gg R_V$, where R_V is the range of the pair-interaction. Eq. (12) can only be solved, however, when g_3 can be expressed in terms of $g(\mathbf{R})$.

The simplest closure is the well known superposition approximation

$$g_3(\mathbf{r}, \mathbf{R}) \; = g(\mathbf{r}) g(\mathbf{R}) g(\mathbf{r} - \mathbf{R}). \tag{14}$$

The problem with this closure is that it does not lead to the Ornstein-Zernike form for the pair-correlation function with a correlation length that diverges at the critical point, because the influence of a third particle on the correlation between the other two particles is neglected. To fix this, we note that the pair-correlation function in the integral in Eq. (13) is multiplied by the pair-force $\nabla V(r)$. Since the range of $\nabla V(r)$ is given by R_V, we need a closure relation only for this small distances $r \leq R_V$. The effect of the presence of the third particle at position $\mathbf{r}_2$ is that it enhances the local density around the two neighboring particles at $\mathbf{r}_1$ and $\mathbf{r}_3$. This density enhancement is equal to

$$\Delta\rho \approx \rho[\, g(\mathbf{R} - \frac{1}{2}\mathbf{r}) - 1] = \rho \, h(\mathbf{R} - \frac{1}{2}\mathbf{r}), \tag{15}$$

where $h = g - 1$ is the total-correlation function. $\mathbf{R} - \frac{1}{2}\mathbf{r}$ is the point in between the positions of particles 1 and 3, so of order $\approx R_V$, relative to the position of particle 2 at a distance $R \gg R_V$. The total-correlation function at these large separations is a very smooth function around zero. Close to the critical point the total-correlation function becomes very long-ranged and decays monotonically, for distances much larger than R_V, to zero. This will be confirmed later. As a consequence, we evaluate the $g(\mathbf{r})$ in Eq. (14) at a density $\rho + \Delta\rho \approx \rho(\mathbf{R} - \frac{1}{2}\mathbf{r})$ at the position in between the two neigboring particles 1 and 3. Since for $\mathbf{R} \gg R_V$ and $\Delta\rho/\rho \ll 1$, we can expand with respect to $\Delta\rho/\rho \ll 1$ to first order, yielding ,

$$g_3(\mathbf{r}, \mathbf{R}) \; = \; \left\{ g(\mathbf{r}) + \frac{dg(\mathbf{r})}{d\rho} \, \rho \, h(\mathbf{R} - \frac{1}{2}\mathbf{r}) \right\} \, g(\mathbf{R} - \mathbf{r}) \, g(\mathbf{R}) \, . \tag{16}$$

This is exactly the relation which was first proposed by Fixman [85].

The final Smoluchowski equation can now be obtained i) by substituting the closure relation Eq. (16) in to Eq. (13); ii) applying a Taylor expansion of $h(\mathbf{R})$ to within linear order, since, as we mentioned before, $h(\mathbf{R})$ is very small for the large separations of interest. This leads to

$$\frac{\partial}{\partial t} \, h(\mathbf{R}) \; = \; 2 \, \beta \, D_0 \, \nabla \cdot \left(\, \nabla \left[\, \frac{d\Pi}{d\rho} \, h(\mathbf{R}) - \Sigma \, \nabla^2 h(\mathbf{R}) \right] \right) \, . \tag{17}$$

We introduced here two new quantities. From the above derivation we find that Π is given by

$$\Pi \;=\; \bar{\rho}\, k_B T - \frac{2\pi}{3}\,\rho^2 \int_0^\infty dr\; r^3\, \frac{dV(r)}{d\,r}\, g^{eq}(r). \tag{18}$$

This is precisely the equilibrium statistcal mechanical well known expression for the osmotic pressure. The second quantity, Σ, is given by

$$\Sigma \;=\; \frac{2\pi}{15}\,\rho \int_0^\infty dr\;\; r^5\, \frac{dV(r)}{d\,r} \left\{ g^{eq}(r) + \frac{1}{8}\,\rho\, \frac{dg^{eq}(r)}{d\rho} \right\} . \tag{19}$$

This is a microscopic expression for the famous Cahn-Hilliard theory free energy square-gradient coefficient.

Equation (17) is the fundamental equation of motion that we will use to analyze the effect of shear flow on long ranged critical structure. In equilibrium $\partial h/\partial t = 0$, this differential equation has a solution (C is a constant),

$$h(R) \;=\; C\, \frac{\exp\{-R/\xi\}}{R}\;, \tag{20}$$

where *the correlation length* ξ is equal to,

$$\xi \;=\; \sqrt{\frac{\Sigma}{d\Pi/d\rho}}\,. \tag{21}$$

According to Eq. (20) for the total-correlation function, the correlation length is a measure for the range over which two spheres interact with each other, via intermediate spheres. Hence it is one of the parameters we set out to determine. Since $d\Pi/d\rho$ vanishes at the critical point, the correlation length diverges as expected. Eq. (21) thus confirms our earlier assumption that at large distances $h(R)$ monotonically decreases smoothly to zero.

In principle $h(R)$ can be measured microscopically. In the case where collective behavior is of interest, however, it is better to chose a scattering approach for experiments, where a full ensemble of particles is probed in reciprocal space. In scattering experiments the structure factor is measured, which is defined as

$$S^{eq}(\mathbf{k}) \;= \frac{1}{N} \sum_{i,j=1}^{N} \langle \exp\{\mathbf{k}\cdot(\mathbf{r_i}-\mathbf{r_j})\}\rangle = 1 + \rho h(\mathbf{k})\;, \tag{22}$$

with $h(\mathbf{k})$ the Fourier transform of $h(\mathbf{r})$. Performing this Fourier transformation of $h(R)$ in eq.(20) we find,

$$S^{eq}(k) \;=\; C\, \frac{4\,\pi}{\xi^{-2}+k^2}\;. \tag{23}$$

Since $S(k=0) = 1/\left[\beta\, d\Pi/d\rho\right]$, the constant C is found to be equal to $1/\left[4\pi\,\beta\,\xi\, d\Pi/d\rho\right] = 1/\left[4\pi\,\beta\,\Sigma\right]$, and hence,

$$S^{eq}(k) \;=\; \frac{1}{\beta\,\Sigma}\; \frac{1}{\xi^{-2}+k^2}\;. \tag{24}$$

This well-known form for the small-wave vector dependence of the structure factor near the critical point is commonly referred to as *the Ornstein-Zernike structure factor*. The Ornstein-Zernike structure factor implies that a plot of $1/S(k)$ versus k^2 is linear, with a slope equal to $\beta\,\Sigma$ and an intercept at $k=0$ equal to $\beta\,\Sigma\,\xi^{-2}$. The above analysis is only valid when the correlation length ξ is much larger than the range of the pair-interaction potential R_V. This imposes, through Eq. (21), in which part of the phase diagram the above theory can be applied, namely where $d\Pi/d\rho$ is very small.

Having derived a microscopic expression for the diverging density fluctuations close to the critical point, we are left with the question about the relaxation dynamics of micro-structural order close to the critical point. This is most conveniently described in terms of the Fourier transformed equation of motion Eq. (17), which reads in terms of the structure factor,

$$\frac{\partial S(\mathbf{k})}{\partial t} \;=\; -2\, D^{eff}(k)\, k^2\; \left[\, S(\mathbf{k}) - S^{eq}(k) \,\right]\;, \tag{25}$$

where S^{eq} is the equilibrium structure factor in eq.(24), and the "*effective diffusion coefficient*" D^{eff} is given by,

$$D^{eff}(k) \;=\; D_0\,\beta\,\left[\,\frac{d\Pi}{d\rho} + \Sigma\,k^2\,\right] \;=\; D_0\,\beta\,\Sigma\,\left[\,\xi^{-2} \,+\, k^2\,\right]\,. \tag{26}$$

The solution of Eq. (25) is $\sim\, \exp\{\,-2\,D^{eff}(k)\,k^2\,t\}$. The effective diffusion coefficient characterizes the relaxation rate of microstructural order with a wavelength equal to $2\pi/k$. The effective diffusion coefficient becomes very small as compared to the single-particle diffusion coefficient D_0 on approach of the critical point, since the correlation length diverges and Σ is well-behaved near the critical point. The dynamics of long wavelength structures (density fluctuations) therefore slows down, which is commonly referred to as *critical slowing down*.

Dispersions of colloidal spheres are ideal to experimentally test the relations Eq. (25) and (26), because attractions between the colloids can be easily induced. In general there are two ways to achieve attractions. The first way is by grafting a small polymer layer on the surface of the colloids so that the particles become attractive when the solvent quality of the polymers is reduced, generally by reducing the temperature. The second way is by adding small polymers to the dispersion that act as depletion agents [86]. Changes in the amount and size of the polymers lead to changes in the range and depth of the interaction potential. It thus has the same effect as that of changing the temperature for most critical systems, such as critical fluid mixtures [87] and polymer dispersions [88]. The phenomena that are described in this section for colloids can also be observed for these systems, which have however a different molecular origin of the critical behavior.

Experiments on mixtures of silica spheres grafted with stearyl-alcohol and Polydimethylsiloxane dispersed in cyclohexane are shown in Fig. 10. These spheres behave as almost perfect hard spheres, while depletion attraction is induced by adding the polymer. The critical point of such systems can be found in two steps. In the first step polymer and colloid concentration are tuned such that the mixture phase separates exactly in an equal amount of the gas phase and the liquid phase. In the second step the system is diluted up to the point that the system does not phase separate any more, which is the critical point. The equilibrium phase diagram is plotted in Fig. 10a. The distance to the critical point can be tuned by first preparing a critical composition ratio of silica to polymer, that phase separates in equal parts of the liquid and fluid phase as indicated by the arrow in Fig. 10. Sequentially, this dispersion can be diluted until the critical point is crossed and concentrated again, approaching the critical point. A schematic Small-angle light scattering (SALS) set-up with which the distance to the critical point can be probed is shown in Fig. 10b. The intensity $I(\mathbf{k})$ measured with SALS is directly proportional to the structure factor $S^{eq}(\mathbf{k})$, as plotted in Fig. 10c, together with a calculated structure factor using Eq. (24) in Fig. 10d. The correlation length ξ, which characterizes the distance to the critical point, can be exactly determined by plotting the reciprocal of the azimuthal averaged intensity $1/I(k)$ vs. k^2, see Eq. (24), as shown in 10e.

B. Non-equilibrium phase behavior

Let us recall that the Péclet number describes the rate of deformation relative to the relaxation rate of the relevant length scale. For individual spherical particles these are the diffusion time D_0 and the radius of the spheres a. For interacting particles the relevant length scale is the range of interaction R_V. Thus, to calculate the relevant bare Péclet number the shear rate needs to be scaled with the time it takes to diffuse over this length scale:

$$Pe \;=\; \frac{\dot\gamma R_V^2}{2D_0}\,. \tag{27}$$

For critical systems the situation changes dramatically. The relevant length scale is now given by the correlation length ξ, while the relaxation rate is given by D^{eff}. When approaching the critical point, these parameters diverge and approach zero, respectively. Hence a new definition of the Péclet number is required that is given by an effective (or, dressed) Péclet number λ that is equal to,

$$\lambda \;=\; \frac{\dot\gamma\,\xi^2}{2\,D^{eff}(k=0)}\,. \tag{28}$$

The question now arises as to how large the actual shear rate $\dot\gamma$ should be to significantly affect the location phase transition lines. First, we note that close to the critical point the dressed Peclet number is very large for shear rates where the bare Peclet number is still small, since $D_{eff} \ll D_0$ and $\xi \gg R_V$. We therefore assume that $g(r)$ for $r \le R_V$, is not affected by the shear flow:

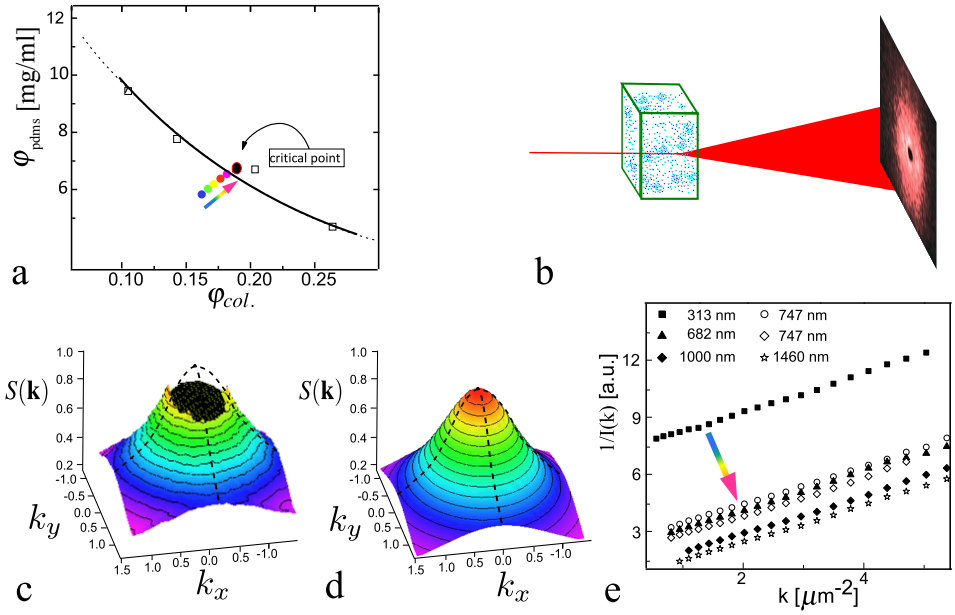

Figure 10: (a) The equilibrium phase diagram of mixtures of silica spheres (102 nm diameter, the x-axis gives the volume fraction φ_{col}) and Polydimethylsiloxane (molecular weight of 206 kg/mol, concentration is given on the y-axis in mg/ml. The range of the interaction potential $R_V \approx 25nm$, since the radius of gyration is 23 nm. The figure is adapted with permission from Ref. [89]. (b) Schematic small-angle light scattering set-up to determine the critical structure (c), which can also be calculated using Eq. (24) (d). The correlation lengths are calculated from the angular averaged structure factors (d), which are schematically shown in (e). The figures (c,d,e) are adapted from Ref. [90]

$$g(\mathbf{r}) \;=\; g^{eq}(\mathbf{r})\,, \tag{29}$$

where g^{eq} is the equilibrium pair-correlation function, that is, the correlation function of the quiescent, unsheared system. Next, a term needs to be added in the original Smoluchowski equation for the probability density function of the ensemble of particles, Eq. (9), which describes the convection of particles in and out of a volume by shear flow. This term is given by $\dot\gamma \sum_{j=1}^{N} \nabla_j \cdot [P\hat{\mathbf{\Gamma}} \cdot \mathbf{r}_j]$, where $\hat{\mathbf{\Gamma}}$ is the deformation tensor as introduced earlier (Eq. (1)). This term translates to $\dot\gamma\, \nabla \cdot \left\{ h(\mathbf{r})\hat{\mathbf{\Gamma}} \cdot \mathbf{r} \right\}$, following the procedure described in the previous section, so that the Smoluchowski equation for $h(\mathbf{R})$ now reads

$$\frac{\partial}{\partial t}\, h(\mathbf{R}) \;=\; 2\,\beta\, D_0\, \nabla \cdot \left(\nabla \left[\frac{d\Pi}{d\rho}\, h(\mathbf{R}) - \Sigma\, \nabla^2 h(\mathbf{R}) \right] \right) - \dot\gamma\, \nabla \cdot \left\{ h(\mathbf{R})\hat{\mathbf{\Gamma}} \cdot \mathbf{R} \right\}\,, \tag{30}$$

which equation of motion is quite similar to that proposed by Onuki [77]. With this equation the coupling between thermodynamics and shear flow is made, within the limits that shear flow is not allowed to be so high that it affects the short-ranged correlations.

Again, Fourier transformation of eq.(30) leads to an expression that can be easily experimentally tested. In steady flow conditions this gives,

$$0 \;=\; \lambda K_1 \frac{\partial S(\mathbf{K})}{\partial K_2} - K^2(1+K^2)\,\left[\, S(\mathbf{K}) - S^{eq}(K) \,\right]\,, \tag{31}$$

where $\mathbf{K} \;=\; \mathbf{k}\,\xi$ is the dimensionless wave vector and the index 1 indicates the flow direction, using the convention given in Fig. 1. The solution of this equation is,

$$S(\mathbf{K}) \;=\; \frac{\xi^2}{\beta\,\Sigma}\, \frac{1}{\lambda K_1} \int_{K_2}^{\pm\infty} dX\;\left(K^2 - K_2^2 + X^2\right)\, \exp\{-F(\mathbf{K}\,|\,X)/\lambda\, K_1\}\,, \tag{32}$$

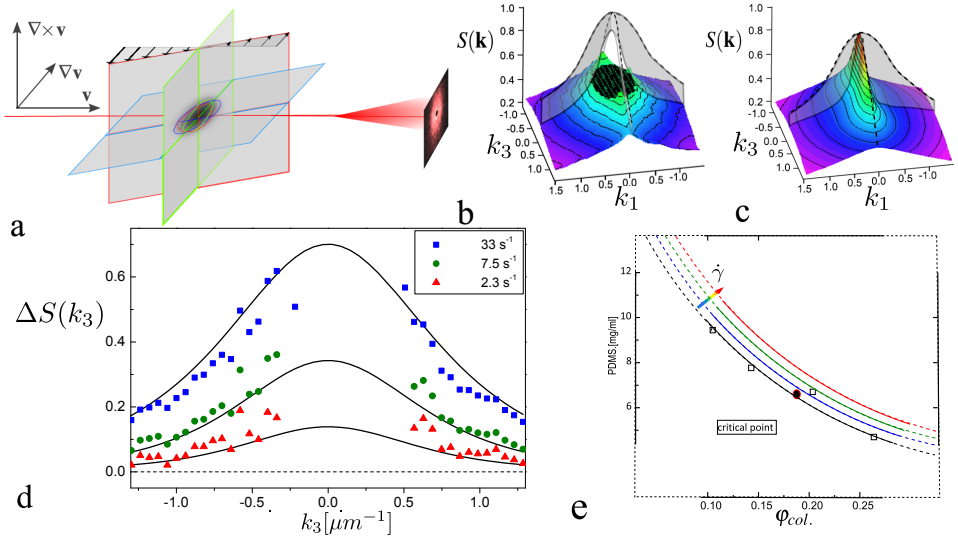

Figure 11: (a) Geometrical set-up of a sheared critical system. The same experimental system is used as in Fig. 6. Experimental (b) and theoretically calculated (c) sheared critical structure factor detected in the flow (1,**v**) and vorticity (3, $\nabla \times \mathbf{v}$) scattering plane. The equilibrium correlation length is 750 nm and the dressed Péclet number is $\lambda = 4$. The shaded surfaces show the difference with the equilibrium structure factor. (d) The difference between the equilibrium and sheared structure factor for different shear rates, taken at the axis where no distortion is expected ($k_1 = 0$). The solid lines are fits to the theory, using Eq. (38). The dashed line indicates the theoretically predicted absence of distortion in this direction. Figure adapted from Ref. [90] © IOP Publishing. Reproduced by permission of IOP Publishing. All rights reserved. (e) Sketch of the effect of shear flow on the phase boundary, adapted with permission from Ref. [89].

with,

$$F(\mathbf{K}\,|\,X) = (X - K_2)\left(K^2 - K_2^2\right)\left(1 + K^2 - K_2^2\right) + \frac{1}{3}\left(X^3 - K_2^3\right)\left(1 + 2K^2 - 2K_2^2\right) + \frac{1}{5}\left(X^5 - K_2^5\right)\left(X^2 - K_2^2\right)\,, \tag{33}$$

where eq.(24) for the equilibrium structure factor has been used. The integration limit in eq.(32) is $+\infty$ when $\lambda K_1 > 0$, and $-\infty$ when $\lambda K_1 < 0$. In order to appreciate the effect of shear flow we plot in Fig. 11 the distortion of the structure factor in terms of

$$\Delta S(\mathbf{K}) = S_{eq}(\mathbf{K}) - S(\mathbf{K}) \tag{34}$$

for experiment, where the system was used as described in Fig. 10, as well as theory.

The distortion of the critical structure factor can be interpreted as suppression of critical fluctuations by convection due to the shear. This distortion only takes place in flow and gradient direction, while the structures in the vorticity direction, where $k_1, 2 = 0$, remain unaltered. The distortion of the critical fluctuations in the flow direction are directly experimentally accessible from the distorted structure factor. This can be seen in Fig. 11b and c, where the shaded areas indicate the difference between the equilibrium and sheared structure factor. The distorted structure factor leads to a diminished correlation length, which, according to the interpretation in the equilibrium phase, reflects an increase in the distance to the critical point. The question is if a system can be further away from the critical point only in specified directions.

Careful inspection of Fig. 11b shows, however, that along the cut $k_1 = 0$ $\Delta S \neq 0$. Fig. 11d clearly shows that ΔS increases with increasing shear rate. This means that there is an overall shear induced shift of the critical point, as schematically shown in Fig. 11e, contrary to the theoretical prediction. Thus, with increasing shear rate the system moves away from the critical point. We now give an argument about the origin of this shear induced shift of the phase boundary.

The core of the argument lies in the assumption we made earlier that the pair correlation function is not affected by shear flow. This assumption is false when the bare Péclet number given by Eq. (27) is around one. To incorporate short ranged distortions, instead of Eq. (29), we expand the correlation function to first order in the bare Péclet

number as,

$$g(\mathbf{r}\,') \;=\; g^{eq}(r\,')\left\{1+\,|\,Pe\,|\;f_0(r\,')-Pe\,\frac{\mathbf{r}\,'\cdot\hat{\mathbf{E}}\cdot\mathbf{r}\,'}{r\,'^2}f_1(r\,')\right\}\;,\;\text{for}\quad r\,'\leq R_V\;, \tag{35}$$

where (the super script T stands for transposition),

$$\hat{\mathbf{E}} \;=\; \tfrac{1}{2}\left[\hat{\mathbf{\Gamma}}+\hat{\mathbf{\Gamma}}^T\right]\;, \tag{36}$$

is the symmetric part of the dimensionless velocity gradient tensor. The functions f_0 and f_1 describe the isotropic and anisotropic response of the short ranged part of the pair-correlation function to shear flow, respectively. The functional form of the anisotropic response can be understood as follows. The velocity gradient tensor can be decomposed as $\hat{\mathbf{\Gamma}}=\frac{1}{2}\left[\hat{\mathbf{\Gamma}}+\hat{\mathbf{\Gamma}}^T\right]+\frac{1}{2}\left[\hat{\mathbf{\Gamma}}-\hat{\mathbf{\Gamma}}^T\right]$. The second term describes a rotational flow, which has no effect on the anisotropy of the structure factor. The first term describes an extensional flow, which gives rise to an increased concentration along the $x=y$ direction and a decrease along the $x=-y$ direction. This is precisely what is described by the anisotropic contribution in eq.(35).

For symmetry reasons, such a linear isotropic distortion must be proportional to the absolute value of the shear rate. This in turn implies that the pair-correlation function for short distances is a non-analytic function of the shear rate. The probable reason for this is that in the equation of motion for g for short distances, integrals containing triplet and four-point correlation functions appear, and these integrals extend over all space. Such integrals also probe the long ranged behavior of g, which is non-analytic in the shear rate. Since close to the critical point such long-range correlations are significant, it might be that these terms give rise to the non-analytic behaviour of g for small distances. The non-analytic form in Eq. (35) is thus probably due to coupling of singularly distorted long ranged correlations to short ranged correlations.

Repeating the analysis leading to Eq. (32), but now using the Ansatz in Eq. (35) instead of assumption (iii) (see Eq.(29)), two additional contributions to Eq.(31) for the structure factor are found,

$$0 \;=\; \lambda K_1\frac{\partial S(\mathbf{K})}{\partial K_2}-K^2(1+\alpha_{iso}+K^2)\,S(\mathbf{K})+K^2(1+K^2)S^{eq}(K)+\alpha_{aniso}\,K_1K_2\,[\,S(\mathbf{K}-1\,]\;, \tag{37}$$

where, as before, $\mathbf{K}=\mathbf{k}\,\xi$ is the dimensionless wave number, and λ is the dressed Péclet number as defined in Eq. (28). There are two new parameters, α_{iso} and α_{aniso}, which can be expressed in terms of integrals of the equilibrium pair-correlation function [90]. α_{iso} measures the susceptibility of isotropic short ranged distortions, and α_{aniso} of the anisotropic distortions.

The solution of eq.(37) is (we use for convenience the same notation for S and F as in subsection IV A, where distortion of short ranged correlations were neglected),

$$\begin{aligned}S(\mathbf{K}) \;=\; \frac{1}{\lambda K_1}\int_{K_2}^{\pm\infty}dX\,\Big\{\left(K^2-K_2^2+X^2\right)\left(1+K^2-K_2^2+X^2\right)S^{eq}\Big(\sqrt{K_1^2+X^2+K_3^2}\Big)\\ -\alpha_{aniso}\,K_1X\Big\}\,\exp\{-F(\mathbf{K}\,|\,X)/\lambda\,K_1\}\;,\end{aligned} \tag{38}$$

with,

$$\begin{aligned}F(\mathbf{K}\,|\,X) \;=\; &(X-K_2)\left(K^2-K_2^2\right)\left(1+\alpha_{iso}+K^2-K_2^2\right)\\ &+\frac{1}{3}\left(X^3-K_2^3\right)\left(1+\alpha_{iso}+2K^2-2K_2^2\right)+\frac{1}{5}\left(X^5-K_2^5\right)-\alpha_{aniso}\,K_1\left(X^2-K_2^2\right).\end{aligned} \tag{39}$$

The integration limits are the same as in eq.(32). Eq. (38) can be used to fit ΔS as is shown by the solid lines in Fig. 11e. The resulting shear rate dependence of α_{iso} is indeed linear. The original equation Eq. (37) is recovered when the short ranged distortions are neglected, so $\alpha_{iso}=0=\alpha_{aniso}$. The finite distortions of long ranged microstructural order for $K_1=0$ is solely due to the coupling to short ranged distortions. The structure factor for wave vectors with $K_1=0$ attains again the Ornstein-Zernike form Eq. (24),

$$S(\mathbf{K}) \;=\; \frac{1}{\beta\,\Sigma}\,\frac{1}{\left(\xi^{eff}\right)^{-2}\,+\,k^2}\quad,\quad(K_1=0)\;, \tag{40}$$

but with a shear-rate dependent "effective correlation length",

$$\xi^{eff} \;=\; \xi/\sqrt{1+\alpha_{iso}}\;. \tag{41}$$

This result confirms the experimental result presented earlier that the overall structure factor is isotropically distorted. We now learn that this is due to local distortions of the local structure, with the effect that the location of the critical point is shifted on applying shear flow, as illustrated in Fig. 11e.

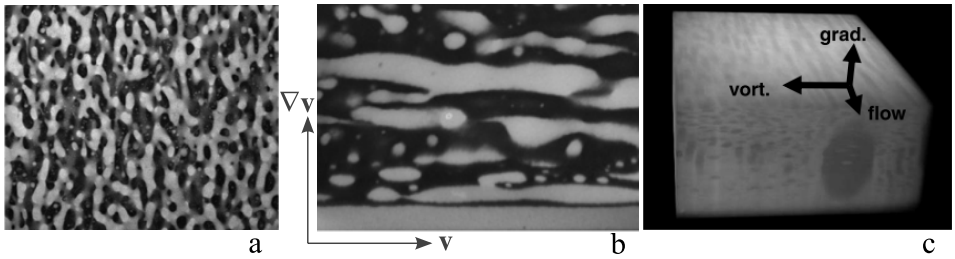

Figure 12: Confocal images of fluorescently labeled PMMA spheres with polystyrene polymers of: (a) an equilibrium phase separating system; (b) the same system under a shear flow of 1.4 s^{-1}. The figures are taken from Ref. [91] © IOP Publishing. Reproduced by permission of IOP Publishing. All rights reserved. (c) 3-D image of a demixing system of a dextran-gelatin dispersion under a shear flow of 9 s^{-1}. Images taken from Ref. [39]. All images were taken using a cone-plate set-up as shown in Fig.6b.

C. The effect on flow behavior

When discussing the effect that dispersions of sticky spheres have on the stability of the flow, one should distinguish between the regime above and below the spinodal line. In other words one needs to know if the system is still mixed but in a state where it is critically slowing down or if the system undergoes spinodal decomposition. For the flow behavior of critical mixtures the main results are based on the work discussed above. Theoretically the viscosity of such dispersions can be calculated as a function of the distance to the critical point. This calculation is involved [84] and will not be presented here. The prediction is, however, that the viscosity more strongly diverges as compared to molecular systems due to long-ranged hydrodynamic interactions between the colloidal particles. Such a strong critical enhancement of the shear viscosity of critical colloidal suspensions has been confirmed in experiments [92]. Flow curves at different points towards the critical point have however not been obtained, although it is very conceivable that such samples are extremely shear thinning, which might result in flow instabilities.

In contrast, there is a vast amount of work done on systems that phase separate in shear flow. The morphology of the structures that are formed during phase separation and the way this morphology is affected by shear flow strongly depends on the composition of the sample and the depth of the quench, which determines the final composition of the two phases [93]. We consider here the simplest case, namely gas-liquid phase separating systems in shear flow, where both phases dynamically behave the same. When a system is quenched just beyond the critical point then initially a bi-continuous structure will be formed: any fluctuation of arbitrary small amplitude and sufficiently long wavelength will continuously grow resulting in spinodal decomposition. The length scale of the fast growing fluctuation is set by the competition between the diffusion which favours small length scales and minimization of density gradient, which favours large length scales. At the moment the interfaces are so sharp that they reach their thermodynamic interfacial tension, capillary forces will drive further coarsening, lowering the free energy by reduction of the total interfacial area [94].

Shear flow will compete with this coarsening process. While the growth rate in the neutral vorticity direction is unhindered, the growth rate in the flow direction coarsening is enhanced by the shear flow. At later times and sufficiently high shear rates the spinodal structure loses its continuous character and no interconnected structures are anymore observed in the gradient and vorticity direction, leading to an anisotropic domain structure. Such stringlike structures have been observed for various systems like binary fluids [95], polymer solutions [96], mixtures of polysaccharides (dextran) and proteins (gelatin) [39], and colloidal sphere-polymer mixture [91] for which we described in section IV C the flow behavior at the stable side of the critical point. For the latter two systems the structures are shown in Fig. 12. The stringlike structures could be considered as small local shear bands, but they do not merge in the gradient nor the vorticity direction. The bands represent a true stable state that is uniquely defined because the same state is reached when quenching from different initial shear rates, both above and below the final shear rate.

The origin of the stability of these structures as well as the shear rate dependence of the diameter of the strings L, given by $L \propto (\dot{\gamma} \cdot \tau)^{-\alpha}$, is still under debate, where τ is related to the growth rate. It is expected that $\alpha = 1$ [91], by balancing the capillary force driven coarsening rate with the shear deformation rate, but for the polymer solution [96] as well as the colloid mixture [91] a much weaker dependence was found of $\alpha \approx 1/3$. In the absence of shear, a long cylinder is unstable against long wavelength undulations and would immediately break up into small droplets [97]. This suggests that the strings can be stable only when undulations of the surfaces, which are prominent due to the low interfacial tension of the systems close the critical point, of the strings are strongly prohibited by shear. The strings are therefore the result of the interplay between hydrodynamic and thermodynamic forces.

At very high shear rates the strings can become as thin as the interface so that the two phases will finally merge.

This has been observed for the polymer solutions [96] as well as liquid mixtures [87, 98]. Thus a homogeneous system is obtained where in quiescent conditions the system would phase separate, so that one can say that the critical point has shifted, as predicted by Onuki [77]. For colloidal systems we discussed this shear induced shift in the previous section, approaching the critical point from the one phase region and not the two phase region as discussed here. Disappearance of the string structure for colloidal systems at high shear rates has not been observed probably because the required shear rates were so high that no stable flow could anymore be guaranteed.

V. EFFECT OF SHEAR FLOW ON THE ISOTROPIC-NEMATIC PHASE TRANSITION OF COLLOIDAL RODS

Almost all molecules, proteins and other types of particles that are present in nature are not spherical. It is therefore appropriate to increase the level of complexity, and move from spherical colloids, as discussed in the last two sections, to rods, which are the simplest non-spherical particles. Compared to spheres, rods have a far more rich phase behavior since rods have both positional and orientational degrees of freedom of the rods. The simplest transition of rod-like particles is the transition from the *isotropic* phase (I), displaying orientational and positional disorder, to the *nematic* phase (N), displaying a mean averaged orientation, but still no long-ranged positional order. Orientational order manifests itself when the dispersion is birefringent due to the difference in the refractive index parallel and perpendicular to the average orientation of the rods. Observations of birefringent structures have been first described by Zocher [99] who studied dispersions of V_2O_5 and FeOOH. These systems consist of inorganic needle shaped particles, as was found by ultramicroscopy, introduced by Zsigmondy in the early 20th century [100]. Not much later, in 1936, similar observations were made on dispersions of Tobacco Mosaic Virus by Bawden et al. [101]. At that time it was surprising that dilute low viscous dispersions of colloidal particles could show birefringence, since birefringence was associated with mineral crystals or thermotropic liquid crystals**, as discussed already in Chapter...**.

It was Onsager who reasoned on the basis of purely geometrical considerations that dispersions of hard rods should also undergo a phase transition from the isotropic phase to the nematic phase [102]. At this phase transition the system will gain positional entropy, since the accessible volume is higher when rods are aligned in the nematic phase, at the cost of orientational entropy. He predicted that this is a first order phase transition with a discontinuity in orientation as well as concentration. As a result there is a concentration range where the isotropic and nematic phases coexist. The concentration and orientational order parameter of the coexisting phases characterize the *binodal* points. These are also the points after which the dispersion becomes metastable to fluctuations in the orientation, when increasing the concentration from an initially isotropic phase or decreasing the concentration from an initially nematic phase. Similarly, spinodal points can be defined and calculated, which mark the concentration where the dispersion becomes unstable and each fluctuation in orientation will result in phase separation.

For dispersions of rods one expects that external fields will affect the behavior even on a single particle level. Where so far we scaled the shear rate with translational diffusion, now the applied field, and therefore the applied torque on the rod, is competing with the rotational diffusion of the rod, orientating the rod when the field is sufficiently strong. This has already been shown in 1902 by Majorana who observed that dispersions of colloidal ferroxides become birefringent when subjected to a magnetic field [103]. Not much later, in 1912, Zocher found that flow could also induce birefringence [104], while Bawden et al. demonstrated the peculiarity of the fact that fluids can show birefringence by publishing a photo of a goldfish in a bowl with tobacco mosaic viruses between crossed polarizers [101]. The obvious question is how alignment induced by an external field influences the location of the I-N transition, since random fluctuations in the orientation are not needed anymore to form a nematic phase from the isotropic phase. In other words, the phase diagram of colloidal rods might change when rods are subjected to an external field. Indeed, studies on rod-like viruses, in this case *fd* virus which we will further introduce later, in a magnetic field showed that the I-N spinodal point shifts to lower concentrations [105]. This means that the external field stabilizes the nematic phase.

In this section we discuss how the isotropic-nematic phase transition is influenced by shear flow. As in the previous sections we start off with a theoretical treatment of the isotropic phase behavior. Again, we use a dynamical approach based on the Smoluchowski equation, which now describes the equation of motion of the orientational probability density distribution. This equation will first be used to determine the I-N and the N-I spinodal points. Next, we will show how the non-equilibrium spinodal lines can be calculated using the same approach, but now including the effect of shear flow on the orientation of the rods. This part is based on Refs. [106, 107] and follows an approach similar to Refs. [108], while similar results were found for thermotropic liquid crystals in shear flow [109].

In order to calculate the binodal lines one has to take the gradients of concentration and orientation at the interfaces into account, as well as the fact that both phase have a different dynamical behavior. Whilst rods in the isotropic phase simply display alignment with increasing shear rate, the flow behavior of the nematic phase is very rich and involves several dynamical transitions [110, 111]. It is predicted that the coexistence of these phases leads to flow-instabilities

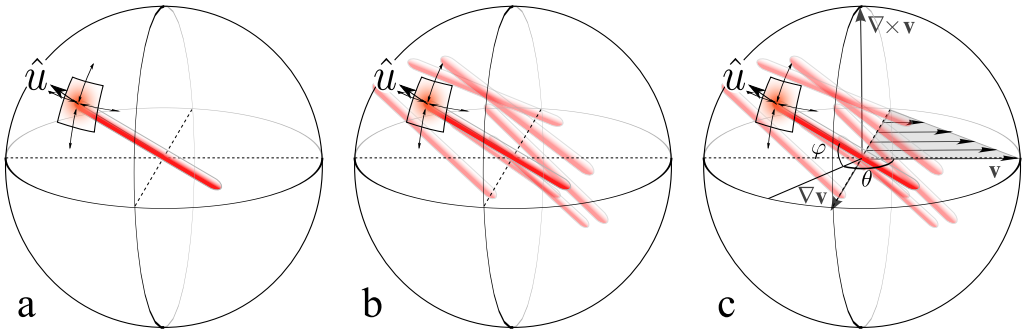

Figure 13: (a) Definition of the unit vector $\hat{\mathbf{u}}$. The arrows out of the little surface area indicate the rotational Brownian diffusion given by the first term in Eq. (42) and Eq. (50). In concentrated solutions (b) neighboring rods exert a torque on the rod, influencing the rotational diffusion given by the second term in Eq. (42) and Eq. (50). Shear flow (c) adds another torque term given by the third term in Eq. (50).

where shear bands can form either in the flow or in the vorticity direction, while the bands consist of the flow-aligning isotropic phase or the nematic phase [11]. As mentioned in section II C, flow instabilities have been observed for many different systems. We choose to restrict our discussion to experiments on almost ideal colloidal rods, the above mentioned *fd* virus, which are extremely slender and relatively stiff. Other systems, especially worm-like micelles, do have features similar to colloidal rods but the origin of flow instabilities can be manyfold and are not necessarily related to the proximity of the I-N transition. We will show how experiments and simulations on colloidal rods can be used to determine the Nematic-Isotropic non-equilibrium spinodal as well as the binodal line that separates the phase coexistence region from the homogeneous mixed phase. It will be shown that the phase coexistence persists as long as the nematic phase is in a tumbling state. Moreover, a flow instability does exist related to the I-N coexistence, but it is different from the theoretically predicted gradient shear bands due to the strong shear thinning close to the non-equilibrium point [11, 107].

A. Equilibrium phase behavior: Isotropic-Nematic phase transition from a dynamical viewpoint

To predict the equilibrium phase behavior we first derive an equation of motion of the relevant order parameter, which we then extend to incorporate the effect of shear flow, as we did for critical colloid-polymer mixtures. In this case we will derive an equation of motion that describes the fluctuations in the orientational distribution function (ODF) of the rods, given by $P(\hat{\mathbf{u}},t)$, since the orientational order parameter changes at the I-N transition. $\hat{\mathbf{u}}$ is the vector that describes the orientation of the long axis of the rod, see Fig. 13a.

Similar to the equation of motion for the probability density function that was used to derive the critical slowing down of attractive colloids, Eq. (9) the Smoluchowski approach will be used to derive the equation of motion of the orientation of the rods:

$$\frac{\partial}{\partial t}P(\hat{\mathbf{u}},t) \;=\; D_r\hat{\mathcal{R}}\cdot\left\{\hat{\mathcal{R}}P(\hat{\mathbf{u}},t) - \beta\, P(\hat{\mathbf{u}},t)\,\bar{\mathbf{T}}(\hat{\mathbf{u}},t)\right\}\;. \tag{42}$$

This equation describes the change in the orientation of the rods along the surface of the unit sphere, which depends on the rotational diffusion of the rods, first term on the right, and the torque exerted on the rods, second term on the right, see Fig. 13b. $\hat{\mathcal{R}}_j$ is the rotation operator given by $\hat{\mathcal{R}}_j\,(\cdots) \;=\; \hat{\mathbf{u}}_j\times\nabla_{\hat{\mathbf{u}}_j}\,(\cdots)$, D_r is the rotational diffusion of the rods at infinite dilution. Similar to the attractive spheres discussed earlier, the torque in equilibrium is due to the interaction with the other rods by (with $\mathbf{R}=\mathbf{r}_1-\mathbf{r}_2$ and $\hat{\mathbf{u}}'=\hat{\mathbf{u}}_2$)

$$\bar{\mathbf{T}}(\hat{\mathbf{u}},t) \;=\; -\bar{\rho}\int d\mathbf{R}\oint d\hat{\mathbf{u}}'\,P(\hat{\mathbf{u}}',t)\,g(\mathbf{R},\hat{\mathbf{u}},\hat{\mathbf{u}}',t)\hat{\mathcal{R}}V(\mathbf{R},\hat{\mathbf{u}},\hat{\mathbf{u}}')\;, \tag{43}$$

where $\bar{\rho}=N/V$ is the number density of rods, $g(\mathbf{R},\hat{\mathbf{u}},\hat{\mathbf{u}}',t)$ is the pair correlation function, and $V(\mathbf{R},\hat{\mathbf{u}},\hat{\mathbf{u}}')$ is the interaction potential between two rods at distance $\mathbf{R}$ and orientations $\hat{\mathbf{u}}$ and $\hat{\mathbf{u}}'$.

The crucial difference with the attractive spheres treated earlier is that the rods have pure hard core interactions. This means that the interaction energy is infinite when the rods overlap and zero when they do not overlap. If the rods are in addition also very long and thin, then it is sufficient to consider only pair interactions. The condition is that the aspect ratio $\frac{L}{d}>100$, where L is the length of the rod and d its thickness. This consideration is the same

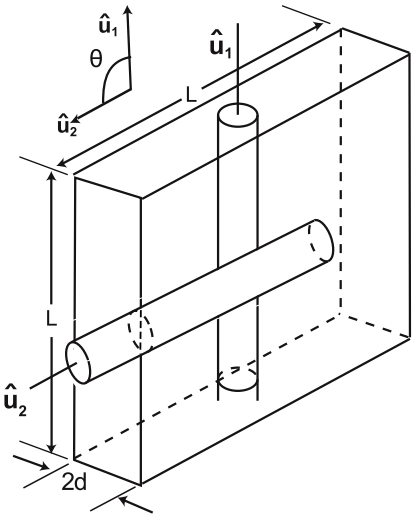

Figure 14: Cartoon of the excluded volume effect in the isotropic phase (which is given by $V_{exc} = \sin(\theta)\, dL^2$.

one that lead to Onsagers prediction for the I-N phase transition. So at this point no closure relation is needed, as it was for the attractive spheres. The integral in Eq. (43) now reduces to

$$\bar{\mathbf{T}}(\hat{\mathbf{u}}, t) \;=\; -\hat{\mathcal{R}}\, V^{eff}(\hat{\mathbf{u}}, t) \;=\; -\hat{\mathcal{R}}\, 2dL^2\beta^{-1}\bar{\rho} \oint d\hat{\mathbf{u}}'\, P(\hat{\mathbf{u}}', t)\; |\,\hat{\mathbf{u}} \times \hat{\mathbf{u}}'\,|\,, \tag{44}$$

where the term $|\,\hat{\mathbf{u}} \times \hat{\mathbf{u}}'\,|$ is a general expression for the volume that is excluded by two rods, see Fig. 14. *The effective potential* V^{eff} is commonly referred to as *the Doi-Edwards potential*, but goes back to Onsager.

The ODF can generally not be measured directly. Therefore we need to relate it to a measurable quantity. Moreover, later on we want to relate the degree of ordering with the stress in the system when it is sheared. Both the ordering and the stress need to be described by tensors. The ordering tensor $\mathbf{S}$ is defined by an integral over the dyadic product $\hat{\mathbf{u}}\hat{\mathbf{u}}$,

$$\mathbf{S} = \oint d\hat{\mathbf{u}}\; \hat{\mathbf{u}}\hat{\mathbf{u}} P(\hat{\mathbf{u}}, t). \tag{45}$$

In experiments often a scalar is measured, for example the birefringence of a sample which gives the scalar S as defined in Eq. (**1.1 in the chapter of Lagerwall**). Here we use λ which is the highest eigenvalue of $\mathbf{S}$, $\lambda = 2\pi \int_0^\pi \cos(\theta)^2 P(\theta)\sin(\theta) d\theta$. For perfectly parallel rods $\lambda = 1$, while in the isotropic phase $\lambda = \frac{1}{3}$. Instead of λ, the scalar order parameter $S = \frac{3}{2}(\lambda - \frac{1}{3})$ is often used, which is 0 in the istropic state and 1 for perfect alignment. Note that S is the same as the average over the second Legendre polynomial P_2.

An equation of motion for the ordering tensor S can now be found using Eq. (44) in Eq. (42) with a proper expansion for $|\,\hat{\mathbf{u}} \times \hat{\mathbf{u}}'\,|$, and operating on both sides of Eq.(42) with $\oint d\hat{\mathbf{u}}\,(\hat{\mathbf{u}}\hat{\mathbf{u}})$ following Doi and Edwards, see Ref. [112]:

$$\frac{d}{dt}\mathbf{S} = -6D_r \left\{ \mathbf{S} - \tfrac{1}{3}\hat{\mathbf{I}} + \tfrac{L}{D}\varphi \left(\mathbf{S}^{(4)} : \mathbf{S} - \mathbf{S}\cdot\mathbf{S} \right) \right\}\,, \tag{46}$$

As in the equation of motion of the pair correlation function of attractive spheres, Eq. (12), there is an unknown parameter on the right side, in this case $\mathbf{S}^{(4)} = \oint d\hat{\mathbf{u}}\; \hat{\mathbf{u}}\hat{\mathbf{u}}\hat{\mathbf{u}}\hat{\mathbf{u}} P(\hat{\mathbf{u}}, t)$. Hence, at this point a closure relation is needed. The simplest closure relation is $\mathbf{S}^{(4)} = \mathbf{SS}$. As we will discuss later, this closure can lead to wrong results, when applying shear. In equilibrium, however, it works fine. To find the I-N transition we seek for a small fluctuation $\delta\lambda$ in the ordering around homogeneous isotropic state, where $\lambda = \frac{1}{3}$. Only considering first order terms in $\delta\lambda$ results in an equation of motion for the perturbation of the stationary state,

$$\frac{d\delta\lambda}{dt} \;==\; -6D_r \left\{ 1 - \frac{1}{4}\frac{L}{d}\phi \right\} \delta\lambda \;=\; -6D_r^{eff}\delta\lambda\,. \tag{47}$$

Here D_r^{eff} is the effective rotational diffusion coefficient,

$$D_r^{eff} = D_r \left\{ 1 - \frac{1}{4}\frac{L}{d}\varphi \right\} . \tag{48}$$

The solution of this equation of motion for the orientational order parameter is now simply given by

$$\delta\lambda(t) \ = \delta\lambda(t=0) \ \exp\left\{-6D_r^{eff}t\right\} . \tag{49}$$

This equation shows how fast a fluctuation in the local ordering will be randomized by the rotational diffusion of the rods. Eq. (49) contains important information about the phase behavior of the rods. It shows namely that $D_r^{eff} \to 0$ when $\varphi\frac{L}{d} \to 4$. Hence, this system shows critical slowing down of the collective rotational diffusion. Fluctuations will grow and the aligned nematic phase is formed into the isotropic phase when $D_r^{eff} > 0$. Note the similarities between the attractive spheres and the hard rods. For both systems an effective diffusion coefficient can be defined (compare Eq. (48) with Eq. (26)), which approaches zero at the phase transition.

The isotropic-nematic spinodal point where $D_r^{eff} = 0$ is found at the scaled concentration $\varphi\frac{L}{d} = 4$. The results agree with the original thermodynamic approach of Onsager [102]. This is not surprising given that the same assumptions were made for the interaction potential between the particles. The equilibrium bifurcation diagram is calculated and plotted as thick lines in Fig. 15a. It is given by the highest eigenvalue λ of stable stationary solutions S_0 versus the concentration, similar to Ref. [113]. Interestingly, the isotropic-nematic spinodal point is located at a higher volume fraction than the nematic-isotropic spinodal point, which is the volume fraction where the homogeneous nematic phase becomes unstable upon diluting concentration. The binodal points could in principle be calculated from a similar Smoluchowski approach for inhomogeneous systems, but this has so far not been done. The reason is that this approach considers fluctuations in a homogeneous background phase, whereas the binodal points describe phase coexistence between phases with different concentration and orientation.

B. Non-equilibrium phase behavior of sheared rods: theory

In order to calculate the non-equilibrium phase behavior of dispersions of colloidal rods, different aspects need to be taken into consideration. First, shear induced alignment is expected to enhance the I-N phase transition. Second, the different dynamical behavior of the isotropic and nematic phase needs to be considered. To start off, the shear term needs to be introduced in the equation of motion of the ODF, giving

$$\frac{\partial P(\hat{\mathbf{u}},t)}{\partial t} \ = \ D_r \, \hat{\mathcal{R}} \ \cdot \left\{ \hat{\mathcal{R}} P(\hat{\mathbf{u}},t) + \ DL^2\bar{\rho}P(\hat{\mathbf{u}},t)\hat{\mathcal{R}} \ \oint d\hat{\mathbf{u}}' P(\hat{\mathbf{u}}',t)|\hat{\mathbf{u}}' \times \hat{\mathbf{u}}| \right\} - \dot{\gamma}\hat{\mathcal{R}} \cdot P(\hat{\mathbf{u}},t)\hat{\mathbf{u}} \times \left(\hat{\mathbf{\Gamma}} \cdot \hat{\mathbf{u}} \right) . \tag{50}$$

The last term in Eq. (50), the shear term, describes the rotation of the rods out of the small surface area due to the applied torque, as indicated in Fig. 13c. This equation again forms the basis for the prediction of the non-equilibrium phase diagram.

The *spinodal* lines can now be calculated in a similar way as the derivation of the spinodal points in equilibrium, using a range of fixed shear rates $\dot{\gamma}$. Again both sides of Eq. (50) are multiplied with $\hat{\mathbf{u}}\hat{\mathbf{u}}$ and the integral is taken to yield the equation of motion for the orientational ordering tensor,

$$\frac{d}{dt}\mathbf{S} = -6D_r \left\{ \mathbf{S} - \tfrac{1}{3}\hat{\mathbf{I}} + \tfrac{L}{D}\varphi \left(\mathbf{S}^{(4)} : \mathbf{S} - \mathbf{S}\cdot\mathbf{S} \right) \right\} + \dot{\gamma} \left\{ \hat{\mathbf{\Gamma}} \cdot \mathbf{S} + \mathbf{S} \cdot \hat{\mathbf{\Gamma}}^T - 2\mathbf{S}^{(4)} : \hat{\mathbf{E}} \right\} . \tag{51}$$

This equation was first put forward by Hess [114]. To proceed from this equation, again a closure relation is needed, expressing $\mathbf{S}^{(4)}$ in terms of $\mathbf{S}$. Compared to the equilibrium case, the final result depends much more on the chosen closure.

The following closure proved to be quite accurate [107],

$$\mathbf{S}^{(4)} : \mathbf{M} = \langle \hat{u}\hat{u}\hat{u}\hat{u} \rangle : \mathbf{M} = \frac{1}{5}\{ \mathbf{S}\cdot\bar{\mathbf{M}} + \bar{\mathbf{M}}\cdot\mathbf{S} - \mathbf{S}\cdot\mathbf{S}\cdot\bar{\mathbf{M}} - \bar{\mathbf{M}}\cdot\mathbf{S}\cdot\mathbf{S} + 2\mathbf{S}\cdot\bar{\mathbf{M}}\cdot\mathbf{S} + 3\mathbf{S}\mathbf{S} : \bar{\mathbf{M}} \} . \tag{52}$$

Here it is used that $\mathbf{S}^{(4)}$ occurs in Eq. (51) in the doubly contracted form,

$$\mathbf{A} \equiv \mathbf{S}^{(4)} : \mathbf{M} \,, \tag{53}$$

where the second order tensor $\mathbf{M}$ is either equal to $\mathbf{S}$ or $\hat{\mathbf{E}}$ and $\bar{\mathbf{M}}$ is the symmetric part of $\mathbf{M}$,

$$\bar{\mathbf{M}} \equiv \frac{1}{2}(\mathbf{M} + \mathbf{M}^T) \,. \tag{54}$$

The stress tensor Σ_D, describing the macroscopic response to shear flow, can be calculated once the orientational ordering tensor $\mathbf{S}$, describing the microscopic state of the rods, is known. This relation is given by the Doi-Edwards relation

$$\mathbf{\Sigma}_D = 2\,\eta_0\,\dot{\gamma}\,\hat{\mathbf{E}} + 3\bar{\rho}k_BT\left[\mathbf{S} - \tfrac{1}{3}\hat{\mathbf{I}} + \tfrac{L}{D}\varphi\,\left[\mathbf{S}^{(4)} : \mathbf{S} - \mathbf{S}\cdot\mathbf{S}\right\} + \tfrac{1}{6}Pe_r\left\{\mathbf{S}^{(4)} : \hat{\mathbf{E}} - \tfrac{1}{3}\hat{\mathbf{I}}\mathbf{S} : \hat{\mathbf{E}}\right\}\right] \tag{55}$$

The first term gives the solvent contribution to the stress, the second term the contribution of the individual rods, the third term the contribution of the interaction between the rods, while the last term is the extra stress as caused by the deformation of the flow field. Since a tensor cannot be measured, measurable scalar numbers need to be extracted, as was the case with the orientational ordering tensor. The most prominent scalar is the shear stress σ_{12}, as was introduced in section II A, because it is the easiest to measure.

To obtain *the spinodal points in shear flow*, first the stationary solution $\mathbf{S}_0$ of Eqs. (51) and (52) needs to be calculated for a finite value of $\dot{\gamma}$, which is done numerically. The reason is that the highest eigenvalue of $\mathbf{S}$, λ, is higher than its isotropic value because shear flow will induce some alignment, so $\lambda > \frac{1}{3}$. Therefore the sheared isotropic phase is called the para-nematic phase. Of course also the ordering of the nematic phase will be influenced by shear flow. Next, the stability of the solution is tested by analyzing if fluctuations around S_0 grow or vanish, as in Eq. 47, while approaching a spinodal line $D_r^{eff} \to 0$. Non-equilibrium bifurcation diagrams can be calculated following this procedure, as shown in Fig. 15a, for various values of the bare Péclet number Pe_r, which is the shear rate scaled by the rotational diffusion of the rods D_r:

$$Pe_r = \dot{\gamma}/D_r \,. \tag{56}$$

The non-equilibrium spinodal lines, depicted in Fig. 15b, are obtained by plotting the end points of the nematic and para-nematic branches. The para-nematic - nematic and the nematic - para-nematic spinodal lines meet at a shear rate of $Pe_r^{crit} = 0.159$ and a scaled volume fraction $\frac{L}{d}\varphi_{crit} = 4.281$. At this point the para-nematic phase can, in principle, be continuously transformed into the nematic phase, and vice versa, by simultaneously changing the concentration and shear rate. Therefore this point defines the *non-equilibrium critical point*. This is a very important concept for sheared dispersions. At this point the shear forces are so large that rod-rod interactions are not able anymore to induce a discontinuous transition. This effect can be quantified by defining an effective rotational Péclet number as

$$Pe_{eff} \;=\; \dot{\gamma}_0/D_r^{eff} \,. \tag{57}$$

The fact that $D_r^{eff} \to 0$ close to non-equilibrium critical point indeed suggest dramatic changes in the sample when subjected to shear flow. This is supported by the flow curve that is calculated using Eq. 55, which displays a region where the slope of the stress versus the shear rate is negative ($\frac{\partial\sigma_{12}}{\partial\dot{\gamma}} < 0$), see Fig. 15c suggesting that the flow is unstable. Another important conclusion from Fig. 15b is that the homogeneous nematic phase remains stable up to lower volume fractions when applying a shear flow, while the homogeneous isotropic phase turns unstable at lower volume fractions. Thus we reach the important conclusion that *shear flow acts to stabilize the homogeneous nematic phase, shifting the I-N phase transition.*

Having defined the non-equilibrium spinodal lines, the question rises how to determine the *non-equilibrium binodal lines*. The Smoluchowski approach is not applicable because two phases with different orientation and concentration coexist and therefore gradients in these parameters are very high. A free energy approach has been used to calculate sheared phase coexisting states [11], similar to Onsagers approach to calculate equilibrium binodal points [102]. It is questionable if this approach is appropriate, because energy is continuously dissipated into the system. An additional

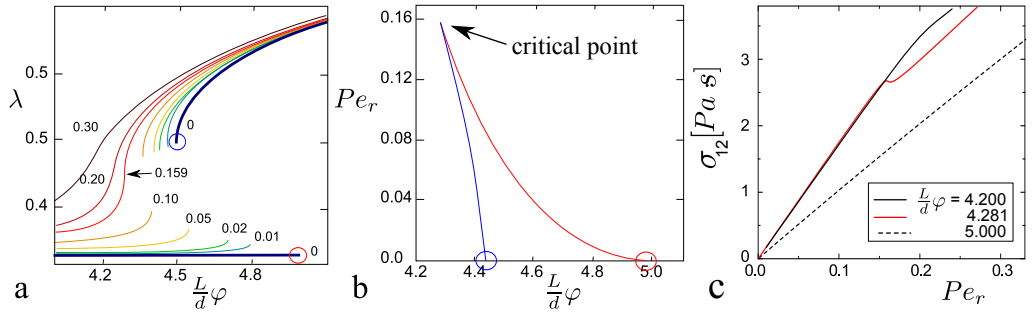

Figure 15: (a) Bifurcation diagram of the nematic order parameter λ, the highest eigen value of stationary solutions of $\mathbf{S}$, vs. the scaled volume fraction $\frac{L}{d}\varphi$, as obtained from the equation of motion Eq. (51) hard rods in shear flow. The numbers refer to values of the bare rotational Péclet number. (b) The non-equilibrium spinodal lines as obtained from (a) by taking the non equilibrium spinodal points. The critical concentration is defined by the point where both spinodal lines meet and given by a critical concentration of $\frac{L}{d}_{crit}\varphi = 4.281$ and critical Péclet number of $Pe_r^{crit} = 0.159$. The circles indicate the equilibrium I-N (red) and N-I (blue) spinodal points and are per definition the end of the isotropic and nematic branch as calculated by Kayser and Raveché [113]. (c) Theoretical flow curves plotting the shear stress σ_{12} vs the bare Péclet number Pe_r. At the critical concentration of $\frac{L}{d}\varphi_r$ the flow curve contains an unstable part where the slope in σ_{12}. Reprinted and adapted from Ref. [107] Copyright 2003, with permission from Elsevier.

problem is that two phases coexist with very different dynamic behavior [11]. While we treated the flow response of the isotropic phase above, the flow behavior of the nematic is very complex and deserves extra attention.

Hess was the first to theoretically show that the nematic director, which defines the average orientation of the rods, undergoes a tumbling motion when a nematic sample is subjected to shear flow [110]. The full 3-D numerical solution of Eq. (50) was first given by Larson [111], where the sequence of dynamic transitions was fully described. The reason for this complex behavior is that the angular distribution of rods in the nematic phase is actually quite wide. Even when the director of the nematic aligns with the flow, a torque will be exerted on the rods in the wings of the angular distribution, which will cause a rotation. While these rods rotate, they drag along the other rods due to the steric interactions, so that a full tumble of the director in the plane defined by the velocity and the velocity gradient vectors will occur. This can be seen in the lower panel of Fig. 16a, which depicts the angle of the director with the flow direction. During the tumble the distribution will widen when $\theta = 45^o$, where the flow is extensional. This can be seen in Fig. 16b, where the orientational order parameter $\langle P_2 \rangle = 0.5(3\lambda - 1)$ is plotted: for $Pe_r = 5.0$, $\langle P_2 \rangle$ approaches zero at regular points during the oscillation. At high shear rates the widening is so drastic that rods will return back to flow axis, as isotropic rods do, so that the director will wag instead of tumble, see dashed line in the upper panel of Fig. 16a. All rods will flow align when the shear rate is so high that it overwhelms the Brownian diffusion, so $Pe_r >> 1$. The sequence of dynamic transitions depends on the degree of ordering of the system and therefore, in the case of lyotropic liquid crystals, on the concentration. The corresponding stress responses, as calculated using the calculated response of $\mathbf{S}$ in Eq. (55), are depicted in Fig. 16c. The very clear oscillations in the stress suggest that rheology is a way to determine if a nematic sample is tumbling, wagging or flow aligning. The problem is, however, that in a sample there are many nematic domains which will undergo oscillatory motions out of phase. In the experimental section we come back to this point, explaining how rheology can nevertheless be used to find the transition between these dynamic states.

We have now described the flow response of both the isotropic and the nematic phase. In order to find binodal lines, another degree of complexity needs to be added to the system, namely the interface between these very differently behaving phases. Due to the complexity of the problem, now satisfactory calculations have been performed so far. To gain a better understanding experiments and simulations are needed, as described in the next paragraph.

C. Non-equilibrium phase behavior of sheared rods: experiment

In principle there are three parameters that are relatively easy to access experimentally: the average orientation using birefringence, concentration differences using scattering, and the stress, using rheology. The protocol to find spinodal and binodal lines is in principle very easy. Prepare a homogeneous dispersion; change the relevant parameters, i.e. concentration or shear rate; determine if the sample phase separates using one of the mentioned techniques. If the system remains homogeneous, then the system is outside the two phase region. If the system immediately phase separates, then it is in the unstable region. If the system phase separates, but after an induction time $\tau_{ind.}$,

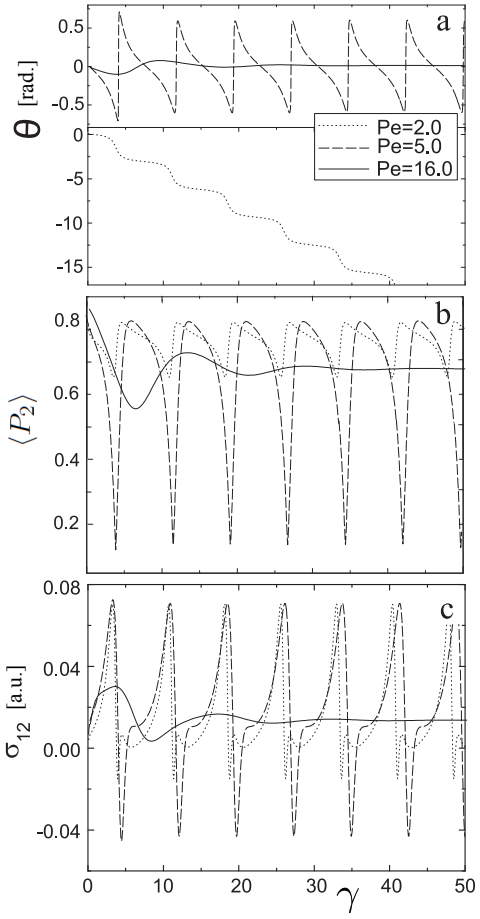

Figure 16: The response of the angle of the nematic director (a), the magnitude of the nematic order parameter(b), and the average stress (c) as a function of strain after a start up of the flow. The dimensionless rod concentration is $\frac{L}{d}\varphi = 4.5$. Data are obtained by numerically solving Eq. (50). The rods are initially placed in the flow-gradient plane. For the stress calculation the solvent contribution was omitted. Reprinted with permission from Ref. [115]. Copyright (2005) American Chemical Society.

then it is metastable. The latter situation was encountered for the crystallization of repulsive spheres, see section III B. Experimentally there are three problems to solve. First, a very reproducible homogeneous state needs to be created. Second, either the concentration or the shear rate need to be changed instantaneously. Third, gradients in orientation or concentration need to be measured. The great advantage of rods is that a homogeneous shear stabilized (para)nematic phase can be easily created by applying shear rates that are so high that all rods align, so $Pe_r >> 1$, while the shear rate can be instantaneously set to another value. Thus the experimental protocol is to prepare a system in the two phase region where isotropic and nematic phase coexist; subject the sample to a very high shear rate for long enough time, so that all structures disappear; quench the system to a low shear rate; observe the sample either by microscopy or light scattering, while measuring the stress if possible.

The only issue now is to find an appropriate system. This is not an easy task since there are many requirements to fulfill for a system to be called a model system. The first requirement stems from Onsagers assumption that only two rods interact at the same time. This is only valid for very slender rods with an aspect ratio of $\frac{L}{d} \approx 100$. We implicitly used this limit also in Eq. (44). Such slender rods do exist, but they will always be somewhat flexible, which means that the persistence length is of the order of the contour length. The other issue is that it is very difficult to have mono-disperse rods with equal length as well as thickness. There is actually only one particle that fulfills most of the requirements, namely bacteriophage *fd* virus. It has a length of $L = 880\ nm$ and thickness of $6.6\ nm$ and it is mono-disperse by nature. At a neutral pH it is charged and somewhat flexible, with a persistence length of around $3\ \mu m$. The charge adds an electro-static repulsion to the interaction, increasing the effective thickness as was already shown by Onsager. The flexibility needs to be accounted for explicitly to have an exact fit with theory for the equilibrium binodal points. A new model particle, which is the same as *fd*, except that one amino acid of the

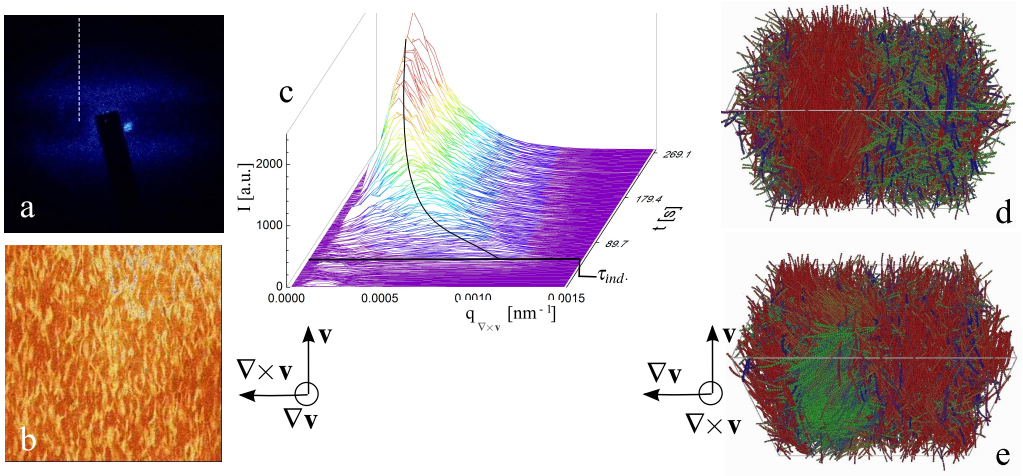

Figure 17: I-N phase coexisting *fd* suspension in shear flow probed by SALS (a) and polarization confocal microscopy (b). Cross section of the scatter pattern (taken at the dashed line in (a)) as a function of time. The size of the form structure can be deduced from this plot as well as the induction time $\tau_{ind.}$. (d) MPCD simulation of a coexisting isotropic-nematic system of rods. The color indicates the orientation. (e) As (d) but now under shear flow. The original nematic phase is undergoing a tumbling motion while the isotropic flow aligns into a para-nematic phase.

more than 2000 coating proteins is changed, has been introduced in 2009. This particle is so stiff that dispersions of it show a complete match with Onsager theory without any fitting [116]. The results presented below, however, use *fd* as a model system, since the experiments were done before 2009 [115, 117]. To facilitate the experiments dextran was added. This is a small polymer which has a radius of gyration similar to the thickness of the rods. The addition of the polymer induces attraction between the rods due to depletion forces, very similar to what was used to obtain the critical systems discussed section IV C. The attraction causes the biphasic region to widen, so that samples between a complete isotropic phase ($\varphi_{nem} = 0$) and complete nematic phase ($\varphi_{nem} = 1$) can easily be prepared.

Fig. 17 shows snap shots of SALS and polarization confocal microscopy experiments on a dispersion of *fd* virus in the I-N phase coexisting region after a quench, i.e. reduction of the shear rate. The bright regions in the microscopy image are elongated nematic droplets in a background of the para-nematic phase. The images were taken using a counter rotating cone plate shear cell as depicted in Fig. 6b. The Fourier transfer of this image is similar to the SALS pattern of the same sample, which was taken using a Couette geometry as in Fig. 6a.

Normally the morphology of the formed structures gives insights in the kind of phase separation that takes place: a bi-continuous structure is formed when the sample phase separates by spinodal decomposition; droplets of the isotropic phase will form when the sample phase separates by nucleation and growth. When phase separation takes place while the sample is sheared, however, very stable, small and elongated structures are formed with interfaces both in the gradient and in the vorticity direction and ill-defined edges in the flow direction, very similar to the shear stabilized bi-phasic gas-liquid structures discussed in section IV B.

Since the sheared system hardly phase separates it is difficult to measure the concentrations of the phase separated sample, so no tie-lines can be constructed to determine the binodal. To determine the spinodal from the morphology of the sheared structures in the non-equilibrium two-phase region is also difficult since there are no clear differences. The best way to determine the Nematic-Isotropic binodal and spinodal is to determine the point, that is concentration and shear rate, where $1/\tau_{ind.} \to 0$ (binodal) and $\tau_{ind.} \to 0$. In the example that is shown in Fig. 17a the cross section of the scatter pattern shows a peak in the intensity that grows and shifts to small q values, indicating that a structure which is initially about the size of a rod length, nucleates at $\tau_{ind.} \approx 30$ s and grows in time, see Fig. 17c. Binodal and spinodal points are plotted in Fig. 18a as solid and open points, respectively, and mark the borders of the unstable region (blue) and the meta-stable region (green). We learn from this diagram that shear flow stabilizes the homogeneous nematic state, since the spinodal line has a negative slope, but *inhibits* the formation of the nematic phase into the para-nematic phase, since the low concentration branch of binodal has a positive slope, contrary to earlier theoretical predictions [11]. The question is now what the origin of the inhibition of the formation of a uniform para-nematic phase is. The answer lies in the behavior of the nematic phase in shear flow.

Information on the tumbling behavior in the nematic phase is obtained by performing flow reversals, where the sign of the shear flow is changed at $t = 0$. This procedure supplies a well defined time at which tumbling of domains is synchronized. At low shear rates only a few oscillations are observed because there are still many nematic domains causing the tumbling to go out of phase, see the green and blue line in Fig. 19 where the response of the viscosity to a

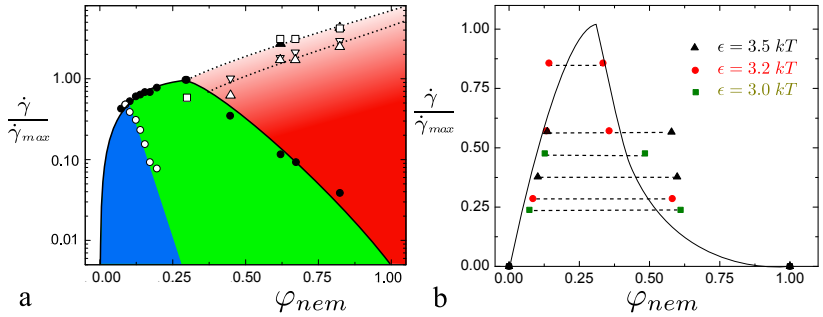

Figure 18: (a) Non-equilibrium experimental phase diagram for *fd* virus with 18 *mg/ml* dextran: binodal (•, solid line is a fit) and N-I spinodal (○) points obtained from SALS; tumbling-to-aligning transition, given by the points where all structures disappear (■) and where the response of the stress after flow reversal is over-damped (□) ; a wagging motion causes a local maximum in the viscosity (▽) and a minimum damping constant (△). The dotted lines are a guides to the eye. The quenched nematic phase is unstable in the blue region and meta-stable in the green region. In the red region the full nematic phase is in a tumbling state. (b) Non equilibrium binodal as obtained from MPCD simulations. The symbols refer to simulations with different depth of the Lennard-Jones potential ϵ causing attractions between the rods. The full line is a fit to the experimental data, as plotted in (a). The dashed lines are the tie lines, connecting binodal points. The shear rate is scaled by the shear rate at the maximum of the binodal, while the *fd* concentration is given in terms of the fraction of the nematic phase in the quiescent sample.

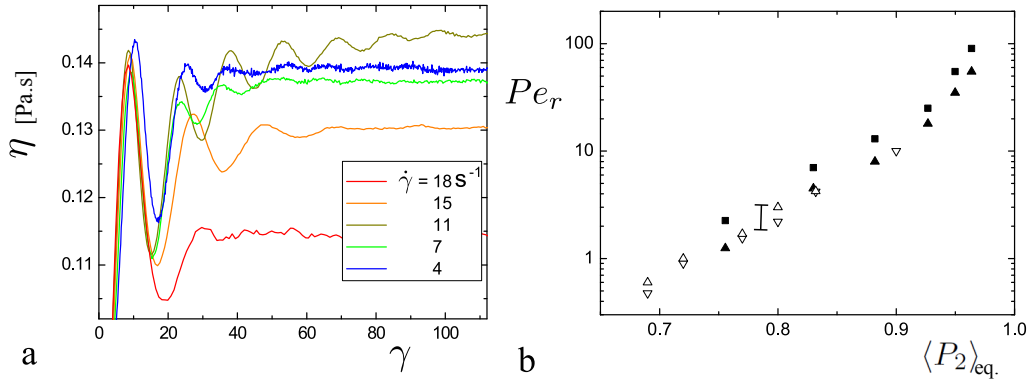

Figure 19: (a) Response of the viscosity after a flow reversal for various shear rates at a concentration nem=0.67. The damping constant first decreases and then increases going towards flow alignment. The time is scaled with the applied shear rate, so the x axis is given in strain units. (b) Dynamic phase diagram of the tumbling nematic phase as a function of the orientational order parameter at equilibrium. The experimental points indicate the Péclet numbers where the viscosity shows a local maximum (▽) and a minimum damping constant (△). The theoretical points indicate tumbling to wagging (▲) and wagging to flow aligning (■) transitions. The region of the transition as inferred from simulations [118] is indicated by the vertical line. Reprinted (adapted) with permission from Ref. [115]. Copyright (2005) American Chemical Society.

flow reversal is plotted versus the acquired strain after reversal. At higher absolute shear rate the damping constant is much less, since more oscillations are observed, while the viscosity is higher, see the olive line in Fig. 19a. These observations comply with a state where structure is almost lost, hence the low damping, while the increased viscosity is a signature of the widening of the orientational distribution as is theoretically predicted by the dashed line for $Pe = 5$ in Fig. 16. The oscillations are again more damped for even higher shear rates accompanied by a drop in the viscosity, confirming the theoretically predicted flow alignment. The bare Péclet numbers where these *dynamic* transitions take place can be plotted as a function of concentration or as a function of the equilibrium orientational order parameter $\langle P_2 \rangle_{eq}$, which is known for *fd* virus [119]. The latter way of plotting allows for a direct comparison with theory and simulations [118], because it is a way to account for the effect of flexibility. The result, plotted in Fig. 19b, shows a very nice agreement between theory and experiment where the shear rate needed to assure flow alignment increases with increasing orientational ordering.

Dynamic transitions as in Fig. 19 can also be found for mixtures that are in phase coexistence in equilibrium as long as the nematic phase dominates the rheological response. These points complete the experimental phase diagram Fig. 18a, bordering a region where the nematic phase is stable but tumbling or wagging (red), and a region where there is a homogeneous flow-aligned state. The fact that the tumbling-to-flow alignment transition line hits the maximum

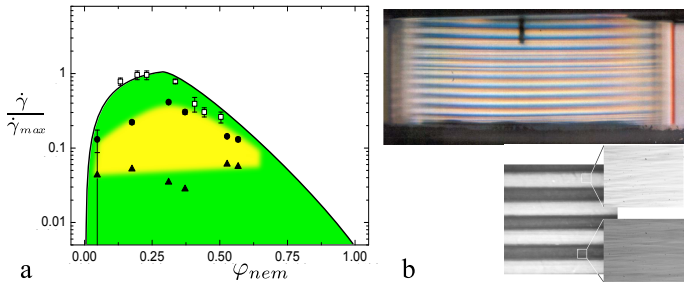

Figure 20: (a) Non-equilibrium binodal for the I-N transition of *fd* virus in shear flow, as Fig. 18a, including the region where vorticity banding is observed. The dextran concentration was 10.6 mg/ml. The binodal line is the same as in Fig. 18a. (b) Macro- and micrographs of vorticity bands all taken with almost crossed polarizers. The top picture shows that bands are formed throughout the couette cell. The hight of the cell being 3 cm. The lower figure shows a banded state for the same where bandwidth is about 2 mm. The two enlargements on the right show the inhomogeneities that are present within the bands.

of the binodal line leads to an important conclusion. It shows that at phase coexistence the nematic phase is always tumbling, since all the binodal points at the high concentration side of the maximum in the binodal lie in the tumbling region. In contrast, the flow aligned para-nematic phase is not tumbling, so that there is on average a huge interfacial tension between the two phase. This interfacial tension only disappears when both phases flow align and display the same dynamic behavior.

This scenario is confirmed by multiple particle collision dynamics (MPCD) simulations, which take the full hydrodynamic interactions into account. Figs. 17d and e show snap shots of an I-N phase coexisting at equilibrium and after applying a shear flow. Contrary to the experiments, the simulation allows for the direct determination of the binodal points at a fixed shear rate, because the local concentration in the two phases can be determined. Before shear flow is switched on a biphasic structure is formed with a nematic layer sandwiched between two isotropic layers. The interface between the two phases does not change position and has the normal in the gradient direction. Due to the size of the simulation box, which is considerable smaller than the length of the bi-phasic structures observed in experiments, one cannot discern if this structure can be categorized as a shear band. It can be observed that the concentration in the para-nematic phase increases, while the concentration in the nematic phase decreases. The final binodal points are plotted in Fig. 18b for different attraction strengths, scaling the shear rate with the shear rate at the maximum of the binodal and the concentration by the volume fraction of the nematic phase in equilibrium. The solid line is the conjectured master curve that also fits the experimental data as plotted in Fig. 18a and binodal points at other dextran concentrations when performing the same scaling. Moreover, it is observed that the nematic phase performs tumbling motion, one of which can be seen in Fig. 17e, up to the point where the phase coexistence disappears, confirming the above sketched scenario.

When comparing the experimental phase diagram (18a) with the theoretical phase diagram (15) for sheared colloidal rods, we notice that the story is not complete. We do not know where to locate the critical point, since the Isotropic-Nematic spinodal line could not experimentally be determined.

D. The effect of the I-N transition on the flow behavior

In deriving the non-equilibrium phase diagram we made the hidden assumption that the flow in the shear cell was linear. This assumption might not be valid since we argued in section II C that flow can become unstable when the sample is extremely shear thinning so that $\frac{\partial \sigma_{12}}{\partial \dot{\gamma}} < 0$. The flow curve that was calculated in section V B for a dispersion of rods at a critical concentration of $\frac{L}{d}\varphi_{crit} = 4.281$ indeed displays such a region, see Fig. 15c. The region where $\frac{\partial \sigma_{12}}{\partial \dot{\gamma}} < 0$ is however very small in shear rate as well as volume fraction and located very close to the critical point. Therefore it is not surprising that in experiments on *fd* virus dispersions as described above no gradient shear banding has been found, not even for a sample in the vicinity of the I-N binodal. It is not possible to produce a more concentrated homogeneous sample, and according to theory this should be the right concentration to obtain the small decline in stress.

On the other hand, bands have been observed that were stacked in the vorticity or neutral direction [40], see Fig. 20b. This vorticity band formation is observed in a limited region *within* the biphasic region, see Fig. 20a, where the sample is microscopically phase separated as shown in Fig. 17. This shear band formation is therefore coupled to the presence of biphasic structures in the dispersion, as we have seen earlier in section IV C for demixing gas-liquid colloid-polymer mixtures. It therefore belongs to the class of systems where vorticity bands formation is connected

to deformation of inhomogeneities, as introduced in section II C. There are however important differences compared to the band formation for gas-liquid colloid spheres-polymer mixtures. The bands that are observed here contain inhomogeneities, whereas in most cases, like for the mixtures discussed in section IV C, the bands consist of a pure phase. Although the exact reason for this shear band formation is unknown, one can argue that the inhomogeneous deformation of the biphasic structures, due to the fact that in couette geometry there is a gradient in shear rate throughout the gap, leads to hoop stresses similar to the Weissenberg effect for polymers.

VI. CONCLUDING REMARKS

This chapter forms an introduction in the field of non-equilibrium phase behavior of colloidal dispersions and the connection with flow instabilities. We first treated the most simple class of dispersions, namely dispersions of hard or repulsive colloidal spheres. These systems crystallize at a critical concentration and we showed that shear flow can enhance as well as frustrate this crystallization, based on early scattering experiments that were recently complemented with confocal microscopy in shear flow. Though concepts of classical nucleation theory are helpful to understand crystallization, they cannot be used to predict this non-equilibrium phase behavior and one has to rely on simulations to support the interpretation of the results.

This situation is different for the second class of dispersions that was discussed, namely dispersions of attractive spheres. For this system we used a microscopic theory based on the Smoluchowski equation of motion on the level of the pair correlation function, which is directly related to the structure factor. The nice feature of the theory is that shear flow can readily be included, while the structure factor can be directly accessed with light scattering. Thus, we could show how the critical point shifts to higher concentrations when applying shear flow by directly comparing theory and experiment.

The most complex system we treated were dispersions of colloidal rods which display an isotropic-nematic phase transition. Again the Smoluchowski approach was used, but now by deriving an equation of motion for the orientation of the particles. The theory predicts that the shear flow stabilizes the homogeneous nematic state, since the spinodal has a negative slope. This was confirmed by confocal and small angle light scattering experiments. These experiments, aided by simulations, also showed that the nematic director tends to tumble while rods in isotropic phase flow align. As a consequence, the sheared nematic and isotropic phase can only merge when rods in both phases are flow aligning. Thus, a non-equilibrium phase diagram is obtained which is very similar to that of crystallizing sphere, with a low concentration branch of binodal that has a positive slope.

Although the selection of subjects was somewhat biased by research in our group, we do think it does nicely illustrate how understanding can be gained for increasingly complex systems. We have shown that knowledge of the micro-structure on the theoretical and experimental level is a prerequisite for the understanding of the non-equilibrium phase behavior and flow of these complex fluids. In real life, that is in industrial applications and in biology, the situation is often much more complex, given the constitution of the substances and the involved flow geometries. We believe, however, that the foundations put out here, are crucial to start understanding more complex situations.

[1] E. W. Merrill, Physiological reviews **49**, 863 (1969).
[2] L. de Viguerie, G. Ducouret, F. Lequeux, T. Moutard-Martin, and P. Walter, C. R. Physique **10**, 612 (2009).
[3] R. G. Larson, *The Structure and Rheology of Complex Fluids (Topics in Chemical Engineering)* (Oxford University Press, USA, 1998).
[4] Z. Cheng, J. Zhu, and P. M. Chaikin, Phys. Rev. **65**, 041405 (2002).
[5] R. Pal, J. of Biomech. **36**, 981 (2003).
[6] W. J. Frith, P. dHaene, R. Buscall, and J. Mewis, J. Rheol. **40**, 531 (1996).
[7] N. J. Wagner and J. F. Brady, Physics Today pp. 27–32 (2009).
[8] C. W. Macosko, *Rheology-Principles, Measurements, and Applications* (Whiley-VCH, 1994).
[9] G. C. Maitland, Curr. Opinion Colloid Interface Sci. **5**, 301 (2000).
[10] M. J. Decker, C. J. Halbach, C. H. Nam, N. J. Wagner, and E. D. Wetzel, Composites Sci. and Tech. **67**, 565 (2007).
[11] P. D. Olmsted and C. Y. D. Lu, Phys. Rev. E **60**, 4397 (1999).
[12] P. D. Olmsted, Europhys. Lett. **48**, 399 (1999).
[13] J. K. G. Dhont, Phys. Rev. E **60**, 4534 (1999).
[14] S. Manneville, Rheol. Acta **47**, 301 (2008).
[15] J. K. G. Dhont and W. J. Briels, Rheo. Acta **47**, 257 (2008).
[16] P. D. Olmsted, Rheol. Acta **47**, 283 (2008).
[17] A. Imhof, A. van Blaaderen, and J. K. G. Dhont, Langmuir **10**, 3477 (1994).
[18] W. M. Holmes, P. T. Callaghan, D. Vlassopoulos, and J. Roovers, J. Rheol. **48**, 1085 (2004).

[19] J. Sprakel, E. Spruijt, M. A. C. Stuart, N. A. M. Besseling, M. P. Lettinga, and J. van der Gucht, Soft Matter **4**, 1696 (2008).
[20] P. Tapadia and S. Q. Wang, Physical Review Letters **91** (2003).
[21] P. Tapadia, S. Ravindranath, and S. Q. Wang, Physical Review Letters **96** (2006).
[22] P. E. Boukany, Y. T. Hu, and S. Q. Wang, Macromolecules **41**, 2644 (2008).
[23] Y. T. Hu, C. Palla, and A. Lips, Macromolecules **41**, 6618 (2008).
[24] N. A. Spenley, M. E. Cates, and T. C. B. McLeish, Phys. Rev. Lett. **71**, 939 (1993).
[25] M. E. Cates, Macromolecules **20**, 2289 (1987).
[26] H. Rehage and H. Hoffmann, J. Phys. Chem. **92**, 4712 (1988).
[27] H. Rehage and H. Hoffmann, Mol. Phys. **74**, 933 (1991).
[28] J. P. Decruppe, R. Cressely, R. Makhloufi, and E. Cappelaere, Colloid Polym. Sci. **273**, 346 (1995).
[29] P. T. Callaghan, M. E. Cates, C. J. Rofe, and J. B. A. F. Smeulders, J. Phys. II France **6**, 375 (1996).
[30] J. B. Salmon, A. Colin, and S. Manneville, Phys. Rev. Lett. **90**, 228303 (2003).
[31] Y. T. Hu and A. Lips, J. Rheol. **49**, 1001 (2005).
[32] E. Miller and J. P. Rothstein, J. Non-Newt. Fluid **143**, 22 (2007).
[33] M. E. Helgeson, M. D. Reichert, Y. T. Hu, and N. J. Wagner, Soft Matter **5**, 3858 (2009).
[34] M. A. Fardin, T. J. Ober, V. Grenard, T. Divoux, S. Manneville, G. H. McKinley, and S. Lerouge, Soft Matter **8**, 10072 (2012).
[35] P. Boltenhagen, Y. Hu, E. F. Matthys, and D. J. Pine, Phys. Rev. Lett. **79**, 2359 (1997).
[36] R. G. Larson, E. S. G. Shaqfeh, and S. J. Muller, J. Fluid Mech. **218**, 573 (1990).
[37] S. Lin-Gibson, J. A. Pathak, E. A. Grulke, H. Wang, and E. K. Hobbie, Physical Review Letters **92** (2004).
[38] F. Pignon, A. Magnin, and J. M. Piau, Phys. Rev. Lett. **79**, 4689 (1997).
[39] R. H. Tromp and E. H. A. D. Hoog, Phys. Rev. E **77**, 031503 (2008).
[40] K. Kang, M. P. Lettinga, Z. Dogic, and J. K. G. Dhont, Phys. Rev. E **74**, 026307 (2006).
[41] P. Pakdel and G. H. McKinley, Phys. Rev. Lett. **77**, 2459 (1996).
[42] M. A. Fardin, D. Lopez, J. Croso, G. Grégoire, O. Cardoso, G. H. McKinley, and S. Lerouge, Phys. Rev. Lett. **104**, 178303 (2010).
[43] M. A. Fardin, T. J. Ober, C. Gay, G. Gregoire, G. H. McKinley, and S. Lerouge, Soft Matter **8**, 910 (2012).
[44] S. M. Fielding, Phys.Rev. E **76**, 016311 (2007).
[45] R. G. Larson, Rheol. Acta **31**, 213 (1992).
[46] B. J. Alder and T. E. Wainwright, Journal of Chemical Physics **27**, 1208 (1957).
[47] D. Frenkel, Physica A: Statistical Mechanics and its Applications **263**, 26 (1999).
[48] W. G. Hoover and F. H. Ree, Journal of Chemical Physics **49**, 3609 (1968).
[49] P. N. Pusey and W. van Megen, Nature **320**, 340 (1986).
[50] T. Palberg, W. Haertl, U. Wittig, H. Versmold, M. Wuerth, and E. Simnacher, The Journal of Physical Chemistry **96**, 8180 (1992).
[51] U. Gasser, E. R. Weeks, A. Schofield, P. N. Pusey, and D. A. Weitz, Science **292**, 258 (2001).
[52] S. Auer and D. Frenkel, Nature **409**, 1020 (2001).
[53] U. Gasser, Journal of Physics-Condensed Matter **21** (2009).
[54] J. K. G. Dhont, *An Introduction to Dynamics of Colloids* (Elsevier, Amsterdam, 1996).
[55] W. B. Russel and A. P. Gast, J. Chem. Phys. **84**, 1815 (1986).
[56] J. Vermant and M. J. Solomon, Journal of Physics-Condensed Matter **17**, R187 (2005).
[57] D. W. Oxtoby, Journal of Physics: Condensed Matter **4**, 7627 (1992).
[58] W. B. Russel, Phase Transitions **21**, 127 (1990).
[59] J. K. G. Dhont, C. Smits, and H. N. W. Lekkerkerker, Journal of Colloid and Interface Science **152**, 386 (1992).
[60] K. Schatzel and B. J. Ackerson, Physical Review E **48**, 3766 (1993).
[61] J. L. Harland and W. vanMegen, Physical Review E **55**, 3054 (1997).
[62] B. J. Ackerson, Journal of Rheology **34**, 553 (1990).
[63] P. Holmqvist, M. P. Lettinga, J. Buitenhuis, and J. K. G. Dhont, Langmuir **21**, 10976 (2005).
[64] I. Cohen, T. G. Mason, and D. A. Weitz, Physical Review Letters **93** (2004).
[65] D. Derks, Y. L. Wu, A. van Blaaderen, and A. Imhof, Soft Matter **5**, 1060 (2009).
[66] T. H. Besseling, M. Hermes, A. Fortini, M. Dijkstra, A. Imhof, and A. van Blaaderen, Soft Matter **8**, 6931 (2012).
[67] F. R. Molino, J. F. Berret, G. Porte, O. Diat, and P. Lindner, European Physical Journal B **3**, 59 (1998).
[68] P. Holmqvist, Langmuir **30**, 6678 (2014).
[69] R. Blaak, S. Auer, D. Frenkel, and H. Löwen, Phys. Rev. Lett. **93**, 068303 (2004).
[70] N. Koumakis, A. B. Schefield, and G. Petekidis, Soft Matter **4**, 2008 (2008).
[71] L. B. Chen, M. K. Chow, B. J. Ackerson, and C. F. Zukoski, Langmuir **10**, 2817 (1994).
[72] E. Eiser, F. Molino, G. Porte, and O. Diat, Physical Review E **61**, 6759 (2000).
[73] I. Cohen, B. Davidovitch, A. B. Schofield, M. P. Brenner, and D. A. Weitz, Physical Review Letters **97** (2006).
[74] Y. L. Wu, D. Derks, A. van Blaaderen, and A. Imhof, Proceedings of the National Academy of Sciences of the United States of America **106**, 10564 (2009).
[75] L. S. Ornstein and F. Zernike, Proceedings of the Koninklijke Akademie Van Wetenschappen Te Amsterdam **17**, 793 (1914).
[76] J. W. Cahn, J. Chem. Phys. **42**, 93 (1965).

[77] A. Onuki and K. Kawasaki, Ann. Phys. **121**, 456 (1979).
[78] X. L. Wu, D. J. Pine, and P. K. Dixon, Physical Review Letters **66**, 2408 (1991).
[79] A. Onuki, Physical Review Letters **62**, 2472 (1989).
[80] S. T. Milner, Physical Review E **48**, 3674 (1993).
[81] H. Tanaka, Physical Review E **59**, 6842 (1999).
[82] A. Onuki, J. Phys.: Condens. Matter **9**, 6119 (1997).
[83] J. K. G. Dhont and H. Verduin, J. Chem. Phys. **101**, 6193 (1994).
[84] J. K. G. Dhont, J. Chem. Phys. **103**, 7072 (1995).
[85] M. Fixman, Journal of Chemical Physics **36**, 1965 (1962).
[86] J. N. Israelachvili, *Intermolecular and surface forces : with applications to colloidal and biological systems* (Academic Press, London ; Orlando, Fla ., 1985), ISBN 0123751802 (U.S. alk. paper), 84021556 Jacob N. Israelachvili. ill. ; 24 cm. Bibliography: p. 276-286. Includes index.
[87] D. Beysens, M. Gbadamassi, and L. Boyer, Physical Review Letters **43**, 1253 (1979).
[88] E. Helfand and G. H. Fredrickson, Phys. Rev. Lett. **62**, 2468 (1989).
[89] T. A. J. Lenstra and J. K. G. Dhont, Physical Review E **63**, art. no. (2001).
[90] H. Wang, M. P. Lettinga, and J. K. G. Dhont, Journal of Physics-Condensed Matter **14**, 7599 (2002).
[91] D. Derks, D. Aarts, D. Bonn, and A. Imhof, Journal of Physics-Condensed Matter **20** (2008).
[92] I. Bodnar, H. Verduin, and J. K. G. Dhont, Phys. Rev. Lett. **77**, 5304 (1996).
[93] H. Tanaka, Faraday Discussions **158**, 371 (2012).
[94] P. C. Hohenberg and B. I. Halperin, Reviews of Modern Physics **49**, 435 (1977).
[95] C. K. Chan, F. Perrot, and D. Beysens, Phys. Rev. A **43**, 1826 (1991).
[96] T. Hashimoto, K. Matsuzaka, E. Moses, and A. Onuki, Phys. Rev. Lett. **74**, 126 (1995).
[97] S. Tomotika, Proceedings of the Royal Society of London Series a-Mathematical and Physical Sciences **153**, 0302 (1936).
[98] D. Beysens, M. Gbadamassi, and B. Moncefbouanz, Physical Review A **28**, 2491 (1983).
[99] H. Zocher, Z. Anorg. Allg. Chem. **147**, 91 (1925).
[100] R. Zsigmondy, *Zur Erkenntnis der Kolloide : Ueber irreversible Hydrosole und Ultramikroskopie* (Jena : Fischer, 1919).
[101] F. C. Bawden, N. W. Pirie, J. D. Bernal, and I. Fankuchen, Nature **138**, 1051 (1936).
[102] L. Onsager, Ann. N.Y. Acad. Sci. **51**, 627 (1949).
[103] Q. Majorana, Il Nuovo Cimento **4**, 374 (1902).
[104] H. Zocher, Z. Phys. Chem. **98**, 293 (1912).
[105] J. Tang and S. Fraden, Phys. Rev. Lett. **71**, 3509 (1993).
[106] T. A. J. Lenstra, Z. Dogic, and J. K. G. Dhont, Journal of Chemical Physics **114**, 10151 (2001).
[107] J. K. G. Dhont and W. J. Briels, Colloid Surface A **213**, 131 (2003).
[108] H. See, M. Doi, and R. Larson, J. Chem. Phys. **92**, 792 (1990).
[109] P. D. Olmsted and P. Goldbart, Physical Review A **41**, 4578 (1990).
[110] S. Hess, Zeitschrift Fur Naturforschung Section a-a Journal of Physical Sciences **31**, 1034 (1976).
[111] R. G. Larson, Macromolecules **23**, 3983 (1990).
[112] M. Doi and S. F. Edwards, *The Theory of Polymer Dynamics*, 1986).
[113] R. F. Kayser and H. J. Raveché, Phys. Rev. A **17**, 2067 (1978).
[114] S. Hess, Zeitschrift Fur Naturforschung Section a-a Journal of Physical Sciences **31**, 1507 (1976).
[115] M. P. Lettinga, Z. Dogic, H. Wang, and J. Vermant, Langmuir **21**, 8048 (2005).
[116] E. Barry, D. Beller, and Z. Dogic, Soft Matter **5**, 2563 (2009).
[117] M. Ripoll, P. Holmqvist, R. G. Winkler, G. Gompper, J. K. G. Dhont, and M. P. Lettinga, Phys. Rev. Lett. **101**, 168302 (2008).
[118] Y. Tao, W. K. den Otter, and W. J. Briels, Phys. Rev. Lett. **95**, 237802 (2005).
[119] K. R. Purdy, Z. Dogic, S. Fraden, h. A. Rü, L. Lurio, and S. G. J. Mochrie, Phys. Rev. E. **67**, 031708 (2003).